Materials Characterization 216 (2024) 114247

Contents lists available at ScienceDirect

Materials Characterization

journal homepage: www.elsevier.com/locate/matchar

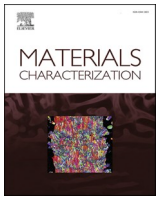

# Nano-scale mechanistic model for microstructural reliability in reactive hybrid solder joints

Farzad Khodabakhshi [a,b,c,*], Irina Wodak [a], Andriy Yakymovych [a], Shabnam Taheriniya [b], Saba Khademorezaian [b], Gerhard Wilde [b], Golta Khatibi [a]

[a] Institute of Chemical Technologies and Analytics, Vienna University of Technology, Getreidemarkt 9/164, A-1060 Vienna, Austria
[b] Institute of Materials Physics, University of Münster, Münster, 48149, Germany
[c] School of Metallurgy and Materials Engineering, College of Engineering, University of Tehran, P.O. Box: 11155-4563, Tehran, Iran

ARTICLE INFO

*Keywords:*
Hybrid solder joint
Reactive Fe-nanoparticles
Intermetallic compound (IMC) layer
Kinetics
Nano-scale characterization
Reliability

ABSTRACT

Hybrid solder joints with upgraded functional performance and reliability were processed by applying reactive Fe-nanoparticles doped into the flux at the interface in order to control and engineer the formation and growth kinetics of the intermetallic compound (IMC) layer. In this framework, the reflow solidification of a Sn- 3.5Ag solder alloy on a copper substrate was studied at high spatial resolution by scanning transmission electron microscopy (STEM) analyses concerning the atomic scale mechanisms underlying the behavior of the reactive iron nanoparticles that were applied at the interface of the solder joint. Elemental mapping distributions displayed the contributing mechanisms suppressing the IMC layer growth by the applied Fe-nanoparticles *via* segregation in front of the $Cu_6Sn_5$ layer, *in situ* reactions to form $FeSn_2$ nanophases distributed inside the $Cu_6Sn_5$ layer and iron elemental diffusion ahead of the $Cu_3Sn$ layer through the lattice of the more extensive IMC layer. These effects of the Fe-nanoparticles that led to a hindrance of the IMC layer growth yielded an energy barrier of up to ~60–70 kJ/mol, thereby effectively stabilizing the solder joint against detrimental phase formation.

## 1. Introduction

Usage of lead free solder joints regarding the considerable developments of the flip-chip technology for different microelectronic packaging issues, like chipsets, graphic cards, micro-processors, and cellular wireless connections ports, exhibited a tremendous industrial application growth over the past two decades [1,2]. The combination of two advanced technologies of chip production and packaging is a new trend for miniaturizing the devices for the demanding requirements of the microelectronics industry [3]. In this context, for industrialization and large-scale manufacturing of electronic connections and assembled devices, soldering is an essential joining technique, with a large ecologically driven trend toward using lead-free materials and avoiding hazardous solders, as well as process miniaturization for accelerating the packaging [4]. For high-performance and safety applications in particular, it is a major challenge to use materials that guarantee long term thermomechanical reliability of the produced solder joints. Mechanical durability/stability and electrical conductivity are two critical functions determining the quality and reliability of the microelectronic interconnections and assemblies. Tin-based solder alloys, as an effective replacement of the well-known Pb—Sn eutectic solder alloy without any environmental issues and toxicity have been developed over the last decades, and their system functionality were assessed by examining different alloying states for use in electronic packaging [5]. In the context of lead-free soldering metallurgy, Sn—Ag and Sn-Ag-Cu are the key systems considering the excellent compatibility with copper as one of the favorable soldering substrate materials with good solderability and well-bonded dilute reaction interfaces between Cu and Sn [6,7].

The typical reflow soldering process, which usually takes several minutes, includes three main steps: eutectic melting of solder alloy, holding at the maximum temperature for the completion of the interfacial reactions, and subsequent cooling to room temperature [8,9]. As a result of the interaction between the molten solder material and the solid substrate interaction, the solder atoms can diffuse through the base metal (and *vice versa*, in cases of super-saturation), resulting in heterogeneous nucleation and formation of intermetallic compound (IMC) layers at the interfaces of solder joints [10]. The formation of such IMC layers is beneficial to improve the wetting of the molten solder on the

* Corresponding author at: Institute of Chemical Technologies and Analytics, Vienna University of Technology, Getreidemarkt 9/164, A-1060 Vienna, Austria.
*E-mail addresses:* farzad.khodabakhshi@tuwien.ac.at, fkhodabakhshi@ut.ac.ir (F. Khodabakhshi).

https://doi.org/10.1016/j.matchar.2024.114247
Received 6 May 2024; Received in revised form 14 July 2024; Accepted 6 August 2024
Available online 8 August 2024

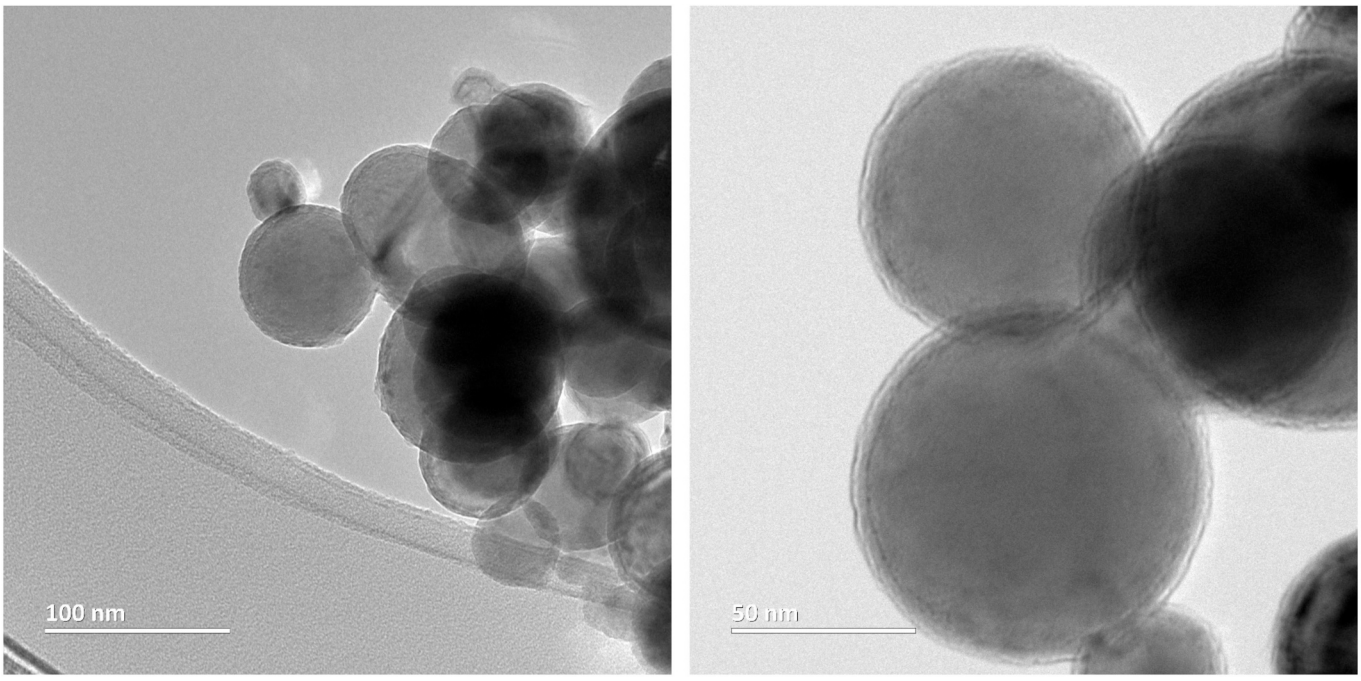


**Fig. 1.** TEM images from the initial Fe-NPs.

copper substrate upon reflow solidification. However, the excessive coarsening during accumulative heating cycles can cause detrimental mechanical failure of solder joints, as they can act as preferred sites for embrittlement and catastrophic cracking [11,12]. Formation of the IMC layers at the interfaces, their composition, growth morphology and progression thickness are critical aspects to control the reliability of solder joints. These aspects need to be analyzed for the three stages of nucleation, growth, and coarsening of the involved interfacial reaction products [13]. In the case of the creation of Cu/Sn interfaces by applying Sn—Ag and Sn-Ag-Cu solder alloys on the substrate of copper, two IMC layers of $Cu_6Sn_5$ and $Cu_3Sn$ may form, with different driving forces and varied states of thermodynamic stability [14].

In various research studies, the experimental characterization and simulation of the formation, stability, and growth of these layers, as well as their impact on compositional and processing parameters, have been extensively explored [15–18]. Furthermore, a crucial aspect for achieving reliable solder joints capable of high-temperature applications in the electronics industry with minimal risk of thermal degradation [19] involves the enhancement of microstructural characteristics of IMC layers and the quality of metallurgical bonds at the interfaces between solder alloys and copper substrates, presenting a continuous area for ongoing research [20].

Following two main strategies for modification of the interfacial IMC layers to maintain the long-term functionality and reliability of solder joints, the effects of different alloying elements [21–23] and secondary phase nanoparticles [24–26] on the formation and growth of IMC layers at the interface between copper substrate and Sn-based solder alloy have been studied. Substitutional alloying for designing SAC + X solders with elements such as Co, Ni and Fe with sufficient solubility in Cu has been shown to promote the suppression of $Cu_6Sn_5$ + $Cu_3Sn$ owing to increased lattice strain caused by alloying [27,28].

In a distinct approach within this field, Hutter et al. [29] explored the incorporation of iron (Fe), cobalt (Co), and aluminum (Al) elements into the flux, which were then mixed with Sn-Ag-Cu solder alloy powder for soldering onto Cu substrates. This study investigated the influence of these elements on the kinetics of formation of $Cu_3Sn$ and $Cu_6Sn_5$ layers at the interface, delving into the underlying interfacial mechanisms. Notably, the introduction of iron and nickel (Ni) led to the formation of two intermetallic layers, $FeSn_2$ and $Ni_3Sn_4$, acting as diffusion barriers against the progressive growth of other intermetallic compound (IMC) layers at the interface with the copper substrate.

Conventional methods for incorporating nanoparticles, both reactive and non-reactive, include mechanical mixing, powder metallurgy, and melting [30]. However, challenges arise with non-reactive ceramic nanoparticles due to their tendency to float upon soldering reflow solidification, stemming from disparities in density and surface energy between the nanoparticles and the molten solder alloy [26,31,32].

The mechanism underlying the incorporation of reactive nanoparticles in the solder involves their dissolution during reflow and subsequent reaction with the solder and substrate, akin to effects observed in micro-alloying [21,22]. This process facilitates the enhancement of solder properties through controlled interfacial reactions, offering potential avenues for improving solder performance in various applications.

An innovative idea for the addition of nanoparticles could be to add these controlling agents particularly at the interface of solder joints instead of mixing them with the solder materials as a more effective strategy [33]. Ghosh et al. [34] followed the strategy of doping reactive particles in the flux, using two types of metallic nanoparticles (*i.e.*, Co and Ni) to control the formation of intermetallic compounds at the Cu/Sn-Ag-Cu interface and possibly suppress their growth kinetics. According to the suggested theories behind changing the interfacial energy between the liquid solder alloy and the surface of the copper substrate by such nanoparticles, the formation of two new stoichiometric compounds of $(Cu, Co)_6Sn_5$ and $(Cu, Ni)_6Sn_5$ were determined and showed strong impact concerning the suppression of the growth kinetics of $Cu_3Sn$ at the interface as a detrimental IMC layer in the structure of solder joints. Furthermore, alongside microalloying and nanoparticle incorporation, an established method for mitigating interfacial intermetallic compound (IMC) growth involves modifying Cu substrates through appropriate coatings. In a recent investigation by Yang et al. [35], the efficacy of stabilizing copper surfaces was explored by applying a nickel-based (Ni-Co-P) electroless coating, aimed at retarding the kinetics of interfacial reactions during IMC layer formation. This intervention led to a notable enhancement in the reliability of solder joints. Microstructural analyses elucidated the formation of $Ni_3Sn_4$,

**Table 1**
Processing conditions regarding the preparation of different solder joints with incorporation of varying iron nanoparticle content at the interface doped into the flux before and after age-annealing heat treatments at various temperatures and times.

| Solder joint | Flux | Fraction of Fe-NPs | Soldering state | Aging treatments (temperature / time) | |
|---|---|---|---|---|---|
| Cu/Sn-3.5Ag/cu | Fe-NPs doped | 0 | Reflowed | 120 °C / 480 h | 180 °C / 480 h |
| Cu/Sn-3.5Ag/cu | Fe-NPs doped | 0.5 *wt*% | Reflowed | 120 °C / 480 h | 180 °C / 480 h |
| Cu/Sn-3.5Ag/cu | Fe-NPs doped | 1.0 *wt*% | Reflowed | 120 °C / 480 h | 180 °C / 480 h |
| Cu/Sn-3.5Ag/cu | Fe-NPs doped | 2.0 *wt*% | Reflowed | 120 °C / 480 h | 180 °C / 480 h |

$Ni_2SnP$, and Ni-Co-Sn thin layers, serving as effective diffusion barriers. Numerous studies have underscored the effectiveness of metallization layers comprising Fe or Fe—Ni films in providing robust diffusion barriers at the solder-pad interface, primarily attributed to the formation of $FeSn_2$ intermetallic compounds [29]. Such strategic modifications at the substrate level hold promise for bolstering the longevity and performance of solder joints in diverse applications.

The primary innovation of the present study lies in the utilization of focused ion beam (FIB) coupled with scanning transmission electron microscopy (STEM) for comprehensive characterization and analysis of intermetallic compound (IMC) layers formed within reactive hybrid solder joints subsequent to reflow solidification and thermal aging modification. The study focuses on elucidating the influence of incorporating reactive iron nanoparticles (Fe-NPs) into the flux and their application at the copper interface during reflow soldering, with Fe-NP weight fractions ranging from 0% to 2%, on the formation, chemistry, morphology, and growth kinetics of altered IMC layers at the solder joint interface. The investigation employs kinetics and thermodynamics-based theories to formulate and elaborate upon these effects.

Furthermore, the study explores the effects of thermal aging, serving as a post-annealing treatment, at two distinct temperatures (120 °C and 180 °C) over extended durations of up to 480 h. The modification of IMC layer stoichiometry and the progressive growth of IMC layers under these conditions are assessed utilizing electron channeling contrast imaging (ECCI) facilitated by field emission-scanning electron microscopy (FE-SEM), providing insights into the structural evolution at the micron-

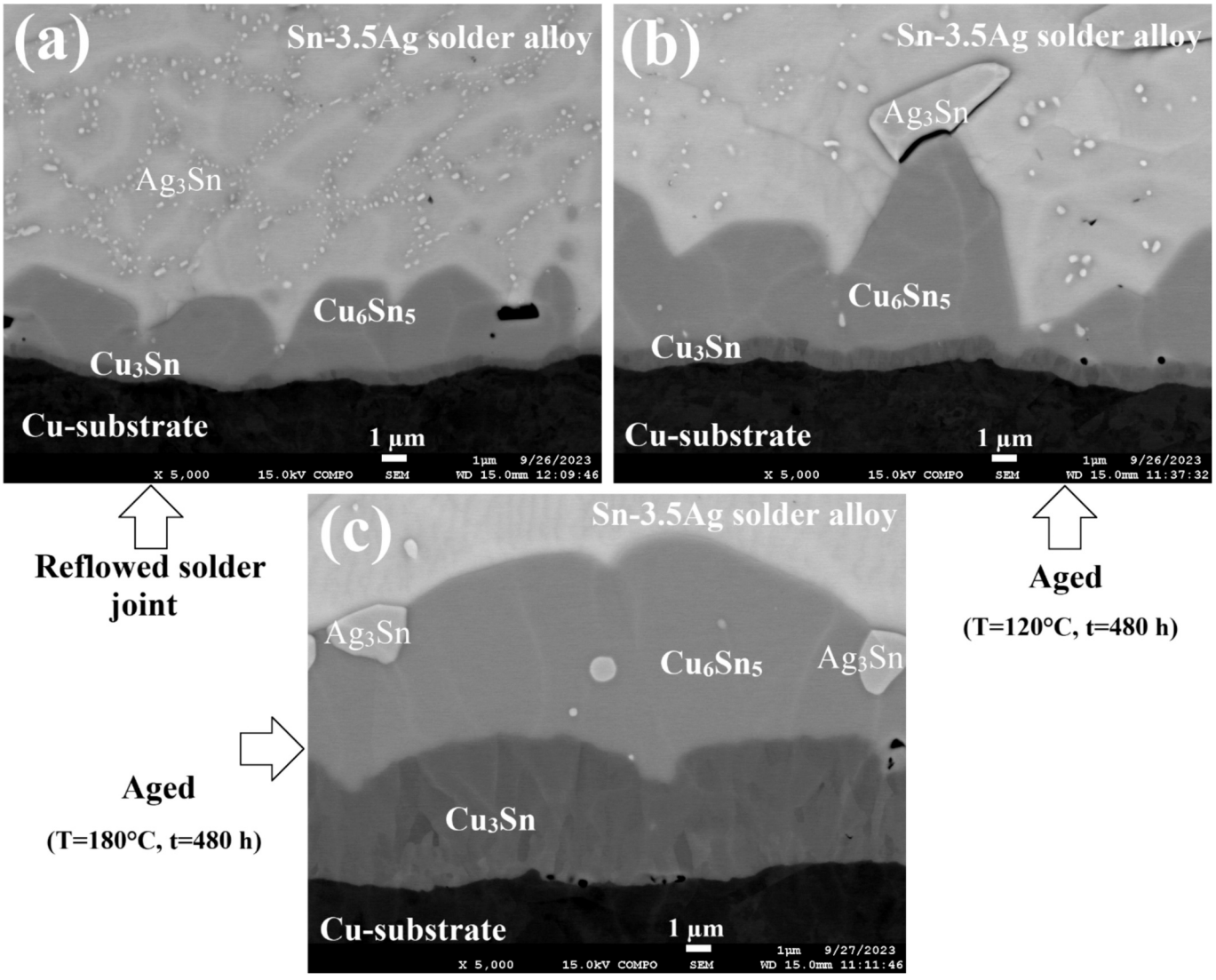


**Fig. 2.** The channeling contrast FE-SEM microstructures for the IMC layers at the interface of the non-reinforced solder joint (0 *wt*% Fe-NPs) under different processing states: (a) Reflowed solder and aging heat treatments at temperatures of (b) 120 °C and (c) 180 °C for 480 h.

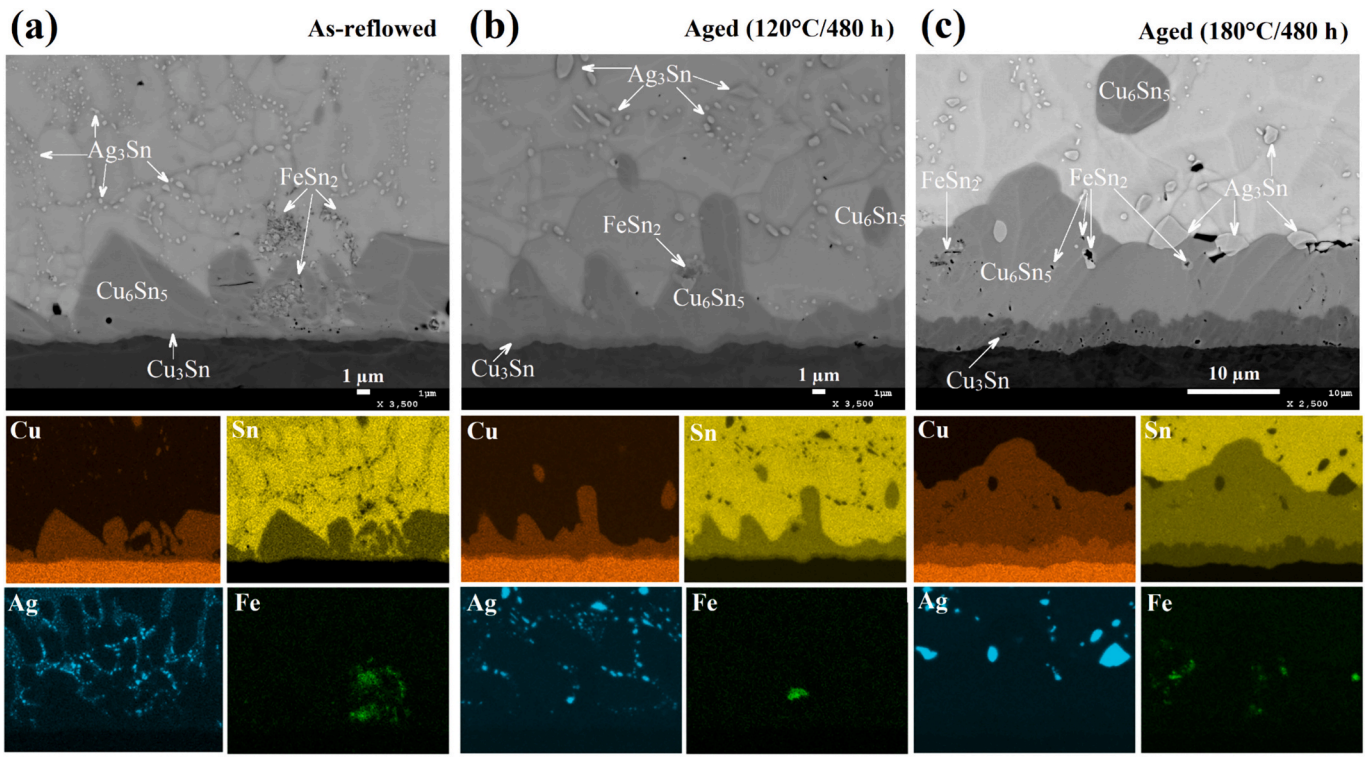


**Fig. 3.** The effects of Fe-nanoparticles incorporation up to ~2 *wt*% on the microstructure of IMC layers by ECCI FE-SEM imaging and the corresponding EDS elemental maps regarding the produced hybrid solder joints after varying (a) reflowed and (b, c) aging processing states: (a) Soldered and (b, c) long times aged at the temperatures of (b) 120 and (c) 180 °C.

level across solder joint cross-sections.

Moreover, the study evaluates changes in mechanical properties of processed hybrid joints in correlation with induced micron-level structural alterations due to reactive nanoparticles and the inhibition of IMC layer growth. This assessment is conducted through nano-indentation hardness mapping experiments performed across various regions of the copper substrate, IMC layers, and the solder alloy area.

Ultimately, the overarching objective of this research endeavor is to propose a nano-scale mechanistic model delineating the concurrent reactive precipitation and development of intermetallic compounds at the interface, aimed at steering the microstructure of hybrid solder joints toward enhanced functional durability and improved reliability.

## 2. Materials and experimental methods

### 2.1. Reactive soldering and hybrid solder joints preparation

For the production of nanoparticle-doped flux, iron nanoparticles (Fe-NPs, Nanografi, purity: 99.55%) were mixed with commercial flux (No-Clean MULTIFIX 450–01, RS Components, Germany) using a planetary centrifugal mixer (THINKY, ARE-250; 2000 rpm. 3 × 2 min) to ensure a uniform dispersion. The iron nanospheres feature an average overall particle diameter of 40–50 nm according to calculations from transmission electron microscopy (TEM) images, as shown in Fig. 1. The oxide layer thickness on the metal core/oxide shell particles was determined to be 5–6 nm using an electron energy loss spectroscopy (EELS) line scan. The content of nanoparticles in the doped flux was varied and amounted to the range of 0–2 *wt*% in relation to the flux.

For microstructure investigations of the hybrid solder joints, copper substrates with a thickness of 2 mm were ground on a *SiC* abrasive paper with a grit size of P600 to remove the oxide layer, and subsequently, residues were eliminated by immersing the ground substrates in an ultrasonic bath containing isopropyl alcohol. Thereafter, sandwich-type samples (Cu-substrate/Fe-NP doped flux/Sn-3.5Ag solder foil/Fe-NP doped flux/Cu-substrate) with four different fractions of Fe nanoparticles (0, 0.5, 1, and 2 *wt*%) were soldered with a deliberate solder gap thickness of 0.2 mm, in a reflow oven (LPKF Zelflow RO4) at 270 °C for 300 s. To ensure a proper soldering process, the samples were preheated at 160 °C for 300 s. Reference samples were prepared similarly with pure flux. After reflow soldering, the samples for microstructure analysis were sectioned across their thickness using a diamond microcutter and embedded in a temperature-stable and conductive mounting material (Technovit® 5000, Sanova, Austria), ground and polished with *SiC* abrasive papers down to P2400 and $Al_2O_3$ (~1 µm), respectively. In addition to the analyses of the as-reflowed solder samples, the microstructure of the samples, which were subjected to the long-time (up to 480 h) thermal aging treatments (MMM Medcenter™ ECOCELL™) at two temperatures of 120 and 180 °C, were also examined. The summary for all processing states and prepared solder joints is expressed in Table 1.

### 2.2. Characterization of the processed hybrid solder joints using advanced electron microscopy techniques

As emphasized before, the innovative and exciting subject of the present project is motivated by applying advanced electron microscopy techniques for the characterization of solder joints to elaborate the submicron mechanisms behind the IMC layer formation and growth upon reflow solidification and thermal aging processes. First, the prepared and treated hybrid solder joints were examined using field emission-scanning electron microscopy (FE-SEM) by optimizing a surface finishing procedure. Then, the interested regions from the IMC layer interface of a specific hybrid joint were selected and considered for further steps to prepare thin lamellas by focused ion beam (FIB) technique and consequently carrying out the high-magnification studies using scanning transmission electron microscopy (STEM).

As addressed above, the leading part of the microstructural assessment was started by thickness sectioning of solder joints following the

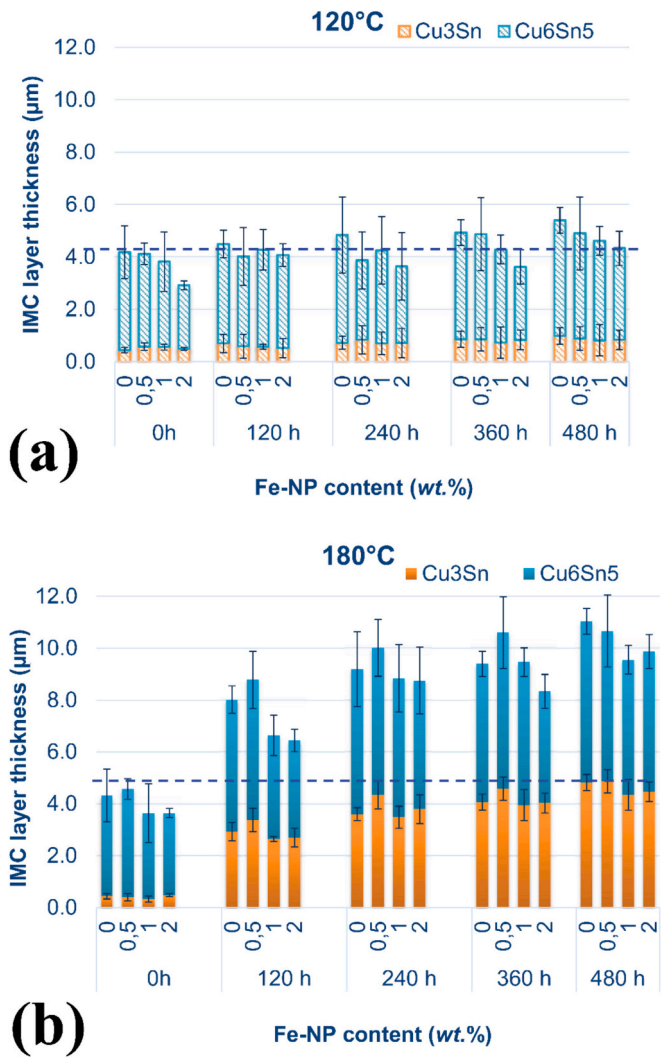


**Fig. 4.** The variations of $Cu_3Sn$ and $Cu_6Sn_5$ IMC layers thicknesses *versus* the aging time of 0 to 480 h for different contents of Fe-NPs, 0 to 2 *wt*%, under two annealing temperatures of (a) 120 and (b) 180 °C.

middle line using a diamond micro-cutter device. After conductive mounting, the sample passed through typical mechanical grinding and polishing steps to achieve mirror-like surfaces. However, two other surface finishing steps were also applied before FE-SEM microscopy after the expressed standard metallographic procedure. At first, using an automatic loading and rotating machine, a chemo-mechanical polishing treatment on the OPS (colloidal silica) suspension for up to 15 min was applied. Afterward, the specimens were placed into the broad-angle ion-milling machine for two hours, and their surfaces were ion-milled. These two final stages exhibited very positive signs in attaining obvious contrast from grain boundaries and interface of precipitates under backscattered electrons imaging mode through the electron channeling contrast imaging (ECCI) concept and also achieving very sharp and in-details chemical maps from the distribution of different Cu, Sn, Ag, and Fe elements in micron-scale undergoing the energy dispersive X-ray spectroscopy (EDS) analysis of FE-SEM microscopy. In this case, a JSM-7600F FE-SEM microscope was utilized as designed by JEOL Company. Hereafter, the morphology and thickness of IMC layers were determined based on FE-SEM backscattering imaging, and their chemistry was analyzed using EDS elemental mapping.

More advanced electron microscopies from the IMC layer were conducted to study the nanoscale features, undergoing FIB/STEM analysis. For this means, a ZEISS FIB-SEM microscopy was employed. With several challenging trials, two lamellas were sectioned across the IMC layer of a hybrid solder joint with ~2 *wt*% of reactive Fe-nanoparticles after age treatment at a temperature of 180 °C for 480 h. Both lamellas were extended upon preparation to be long enough and included all borders at the interface, *i.e.,* the copper substrate, IMC layer, and Sn—Ag solder alloy. However, during subsequent FIB lamella thinning down to the critical size of about 50 nm, in one of the lamellas, the main target for thinning was the interface of the IMC layer with the solder alloy matrix. For the other case, the focus was on reducing the thickness of the interface part between the IMC layer and copper substrate. Accordingly, the STEM observations and EDS elemental map analyses at varying magnifications and for different features were accomplished from the desired thinned regions around the IMC layer. Regarding this substance, an FEI STEM microscope of Titan Themis G3 was operated with the possibility of elevating the accelerating voltage up to 300 keV, and microstructural characterizations performed under three modes of high-angle annular dark-field (HAADF), bright-field (BF), and dark-field (DF) imaging, by STEM analysis.

### *2.3. Nanoindentation experiments across the thickness section of solder joints*

In the case of the mechanical response of the prepared solder joints, the localized properties were assessed using nanoindentation mapping across the soldered areas, including the copper matrix, Sn—Ag solder alloy, and also the IMC layer at the interface. Such experiments were conducted on the previously mentioned solder joints of 0 *wt*% Fe nanoparticles in the reflowed state and nanocomposite one with ~2 *wt*% Fe nanoparticles after long-times aging (480 h) at a temperature of 180 °C. Both specimens for nanoindentation measurements were surface finished according to the typical/standard metallographic sample preparation procedure down to a diamond paste of size ~1 μm. Subsequently, they were fixed on the holder of a FEMTO TOOLS FT-NMT04-XYZ nano-indenter machine for cross-sectional mapping of hardness and modulus variations. A Berkovich tip with a radius of ~20 nm was used for testing, as all nanoindentation experiments were performed with a loading rate of 0.05 μN/s and monitored with a constant penetration depth of 100 nm, following continuous calculation of tested material stiffness. Accordingly, the indentation force was controlled in the 0.5 to $2 \times 10^5$ nN range during such a high-resolution/high-speed mapping. To this end, a working window of 240 μm × 180 μm from the substrate, solder alloy, and IMC layers for both solder joints was selected for testing, and nanoindentation maps were collected with distance intervals of 5.0 μm. By the completion of mapping and consequent calculations, the hardness and reduced modulus contours and distribution profiles, in addition to the average values for each region, were comprehended and demonstrated. Afterward, the nanoindentation impressions and their distributions on the mapped section of soldered joints were further examined and captured using FE-SEM microscopy.

## 3. Results and discussion

### *3.1. Formation of IMC layer across the interface of hybrid solder joints*

In Fig. 2a, the formation of two distinct IMC layers at the interface of Cu/Sn-Ag/Cu hybrid solder joint without any reinforcing agent after reflow solidification is illustrated by ECCI microscopy. As seen, the liquid-solid interfacial reactions resulted in the formation of the thermodynamically stable $Cu_6Sn_5$ compound (η) as a rather thick IMC layer between the solder and Cu substrate, beneath which also a thin layer of $Cu_3Sn$ IMC (ε phase) has already been formed during the reflow process. Also, a fine distribution of round $Ag_3Sn$ intermetallic particles through the solder alloy matrix after reflow soldering is observed, as indicated in Figs. 2 and 3.

As extensively documented in the literature on lead-free soldering [11,36,37], the morphology of the $Cu_6Sn_5$ layer front during the

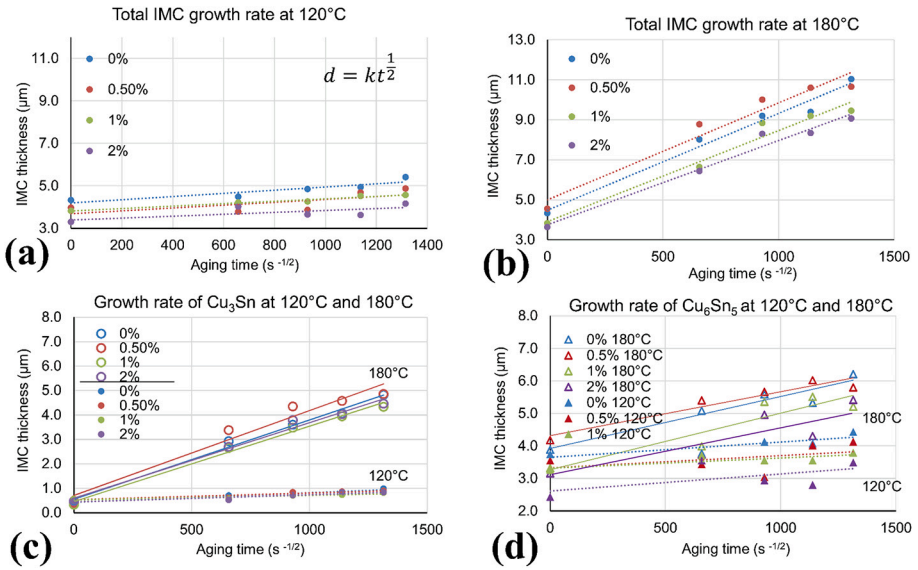


**Fig. 5.** Linear plots of the IMC layer thickness in micron-scale, *d*, changes upon age heat treatment as a function of aging time square root, $t^{0.5}$, for different Fe-NPs contents of 0 to 2 *wt*%. Summation of both $Cu_3Sn$ and $Cu_6Sn_5$ layers thicknesses across the solder joints prepared under two altering aging temperatures of (a) 120 and (b) 180 °C, respectively. The same linear trends for the growth of each (c) $Cu_3Sn$ and (d) $Cu_6Sn_5$ IMC layers separately, and comparing the impact of age heat treatment for two temperatures of 120 and 180 °C together under varying Fe-NPs content.

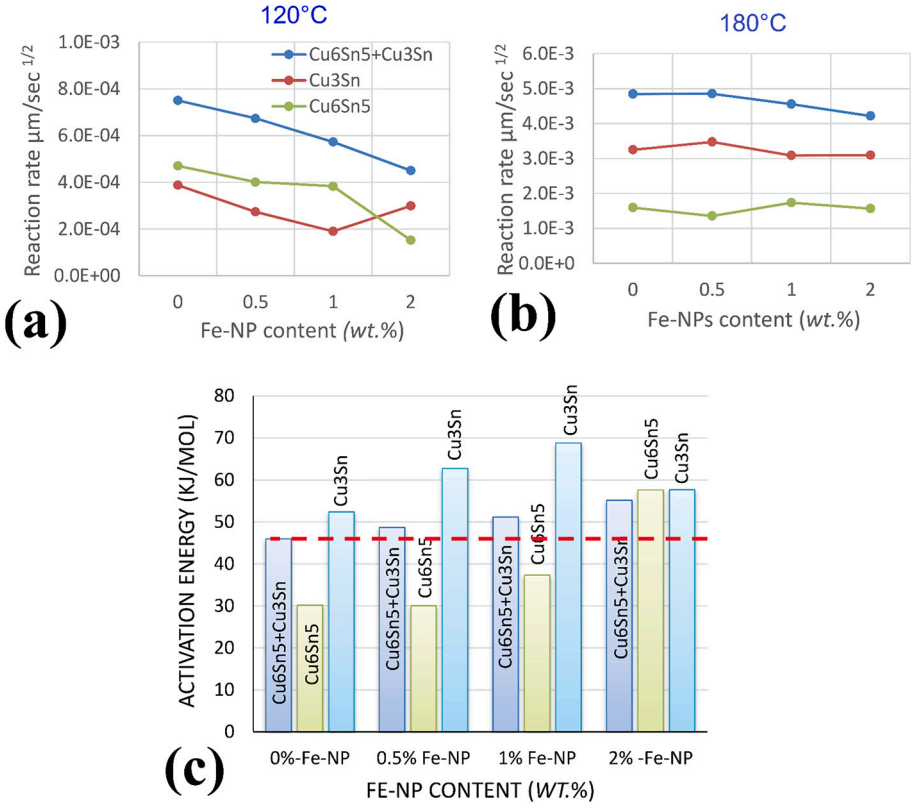


**Fig. 6.** The estimated fields of reaction rates *versus* the content of Fe-NPs for different IMC layers across the solder joint undergoing aging heat treatment at two temperatures of (a) 120 and (b) 180 °C. (c) The calculated activation energies for the progression growth of IMC layers across the interface of hybrid solder joints upon reflow solidification and thereafter aging at different temperatures for varying contents of Fe-NPs.

soldering reflow process exhibits a characteristic scallop-shaped appearance. Additionally, within the solder joint region, a uniform distribution of micron-sized particles comprising $Ag_3Sn$ is prominently observed. Notably, in the context of lead-free solder systems utilizing the Sn—Ag alloy, various morphologies of $Ag_3Sn$ intermetallic compounds can be generated, including spheroidal forms, eutectic lamella structures, needles, and plates, contingent upon solidification directionality and applied cooling rates during processing, as reported in the literature [38].

The formation of fine spheroidal and eutectic distributions of $Ag_3Sn$

**Table 2**
The calculated values of the growth rate constant for the separate and simultaneous formation of IMC layers at two different aging temperatures of 120 and 180 °C for the altered contents of Fe-NPs.

| Sample Cu/Ag3.5Sn/cu | Growth rate constant (D) ($m^2/s$) 120 °C | | | Growth rate constant (D) ($m^2/s$) 180 °C | | |
|---|---|---|---|---|---|---|
| Fe-NP *wt%* | $Cu_6Sn_5$ + $Cu_3Sn$ | $Cu_6Sn_5$ | $Cu_3Sn$ | $Cu_6Sn_5$ + $Cu_3Sn$ | $Cu_6Sn_5$ | $Cu_3Sn$ |
| 0 | 7.50E-16 | 4.70E-16 | 3.88E-16 | 4.84E-15 | 1.60E-15 | 3.24E-15 |
| 0.5 | 6.73E-16 | 4.00E-16 | 2.73E-16 | 4.85E-15 | 1.35E-15 | 3.47E-15 |
| 1.0 | 5.72E-16 | 3.82E-16 | 1.90E-16 | 4.55E-15 | 1.74E-15 | 3.09E-15 |
| 2.0 | 4.50E-16 | 1.51E-16 | 2.98E-16 | 4.21E-15 | 1.57E-15 | 3.09E-15 |

intermetallic particles within the solder alloy microstructure has been linked to enhancements in thermal fatigue and creep resistance. Specifically, the prevalence of eutectic structures predominantly contributes to bolstering the creep strength of the solder joint. Conversely, the literature suggests that the presence of coarser distributions of $Ag_3Sn$ intermetallic phases, characterized by needle- or plate-like morphologies, which typically form at lower solidification cooling rates, has a lesser impact on the reliability of solder connections. These findings underscore the nuanced relationship between intermetallic morphology and solder joint reliability, providing valuable insights for optimizing solder alloy compositions and processing parameters to enhance joint performance in practical applications.

By applying a post annealing heat treatment and increasing the aging temperature up to ~180 °C, the thickness of both $Cu_3Sn$ and $Cu_6Sn_5$ IMC layers continuously increased with a drastic coarsening of the $Ag_3Sn$ precipitates, as displayed in Figs. 2b, c, due to the solid-state elemental diffusion across the solder joint.

The consistent findings across three distinct states—initial as-reflowed material and subsequent to aging heat treatments up to 480 h at temperatures of 120 °C and 180 °C—regarding the hybrid solder joint featuring the incorporation of 2 *wt*% Fe-NPs in the flux are depicted in Figs. 3a-c, respectively. In addition to microstructural characterization utilizing ECCI to elucidate the morphology and grain structure of intermetallic compound (IMC) layers, the chemistry of various compounds within the solder joint was evaluated through EDS elemental mapping of Cu, Sn, Ag, and Fe elements. These comprehensive analyses provide insights into the influence of Fe-NPs addition on both the formation of IMC layers during reflow solidification and their subsequent progressive growth during thermal aging treatments.

A detailed examination of these characterization results reveals that a majority of iron particles are segregated and react within the $Cu_6Sn_5$ layer and its immediate vicinity under the initial as-reflowed state, as depicted in Fig. 3a. This observation underscores the role of Fe-NPs in initiating and influencing interfacial reactions, suggesting a complex interplay between the introduced nanoparticles and the solder matrix during the soldering process.

Through the implementation of post-soldering aging heat treatments at two distinct temperatures, the diffusion range of iron elemental species was substantially augmented across the intermetallic compound (IMC) layer and its immediate vicinity, leading to the formation of *in situ* products characterized by a higher fraction and more uniform distribution. This observed extension in iron diffusion range is indicative of the retarding effect exerted by Fe-NPs on the growth rate and morphology of $Cu_6Sn_5$ and $Cu_3Sn$ during both reflow solidification and subsequent aging steps. Such effects are likely attributed to the intricate interactions between these phases and micro- to nanoscale Fe-rich precipitates, potentially comprising the $FeSn_2$ phase.

A comparative analysis between different regions depicted in Figs. 2 and 3 highlights notable shifts in the growth morphology of the dominant $Cu_6Sn_5$ IMC layer toward a cauliflower-like state, particularly evident under conditions of isothermal aging and incorporation of reactive Fe nanoparticles. Additionally, upon closer examination of microstructural details *via* FE-SEM microscopy as presented in Figs. 2 and 3, the emergence of micron-level voids along the solder joint interface and surrounding the IMC layer, particularly following thermal aging, warrants attention. These voids could be attributed to the Kirkendall effect, arising from elemental interdiffusion between copper and tin during the concurrent formation of IMC layers. This phenomenon has been extensively discussed in the literature concerning solder joints, providing nuanced insights into the underlying mechanisms governing interfacial behavior and morphological evolution in such systems [39].

FE-SEM investigations were performed on the interfacial regions of all prepared hybrid solder joints with different contents of Fe-NPs (0, 0.5, 1.0, and 2.0 *wt%*) after reflow and isothermal aging at 120 °C and 180 °C for various holding times of 0 to 480 h. The measured layer thickness of both $Cu_3Sn$ and $Cu_6Sn_5$ compounds as a function of aging temperature and time, along with the content of reactive Fe-NPs, was used for calculations regarding the formation and growth kinetics of these IMC layers.

An in-depth characterization of the reported effects of Fe-NPs on the growth of IMC layers with the aim of identifying the nano-scale mechanisms responsible for these reactive interactions requires advanced microscopic studies, are presented and discussed in the following sections.

**Table 3**
Comparison between the estimated activation energy ranges for the formation and growth of IMC layers.

| Solder joint/couple | Temeparture range (°C) | Activation energy for formation (kJ/Mol) | | | | | References |
|---|---|---|---|---|---|---|---|
| | | $Cu_6Sn_5$ + $Cu_3Sn$ | $Cu_6Sn_5$ | $Cu_3Sn$ | $(cu,Ni)_6Sn_5$ | $FeSn_2$ | |
| Cu/Sn3.5Ag | 120–180 | 46.0 | 30.2 | 52.4 | | | This work |
| Cu/Sn3.5Ag + 0.5%Fe-NP | 120–181 | 48.7 | 30.0 | 62.7 | | | This work |
| Cu/Sn3.5Ag + 1.0%Fe-NP | 120–182 | 51.2 | 37.3 | 68.8 | | | This work |
| Cu/Sn3.5Ag + 2.0%Fe-NP | 120–183 | 55.2 | 57.6 | 57.6 | | | This work |
| Sn-cu | 130–200 | | 77.6 | 85.4 | | | [49] |
| $Cu/Cu_3Sn$ | 150–200 | | 81.0 | | | | [50] |
| $Cu_6Sn_5/Sn$ | 225–350 | | | 73.8 | | | [50] |
| $Cu/Cu_3Sn/Cu_6Sn_5/Sn$ | 125–200 | | 47.3 | 38.7 | | | [45] |
| Cu/Sn3.5Ag | 70–205 | 64.8 | 48.5 | 89.1 | | | [51] |
| Sn-3.8Ag-0.7Cu | 75–175 | 77.7 | 52.3 | 80.7 | | | [48] |
| Sn-3.8Ag-0.7Cu + 0.27 Ni-NP | 75–176 | 48.4 | 43.1 | 96.4 | | | [48] |
| SAC/cu | 125–175 | | 86.0 | 97.1 | | | [52] |
| SAC/Fe-45Ni | 125–175 | | | | 121.9 | 105.6 | [52] |

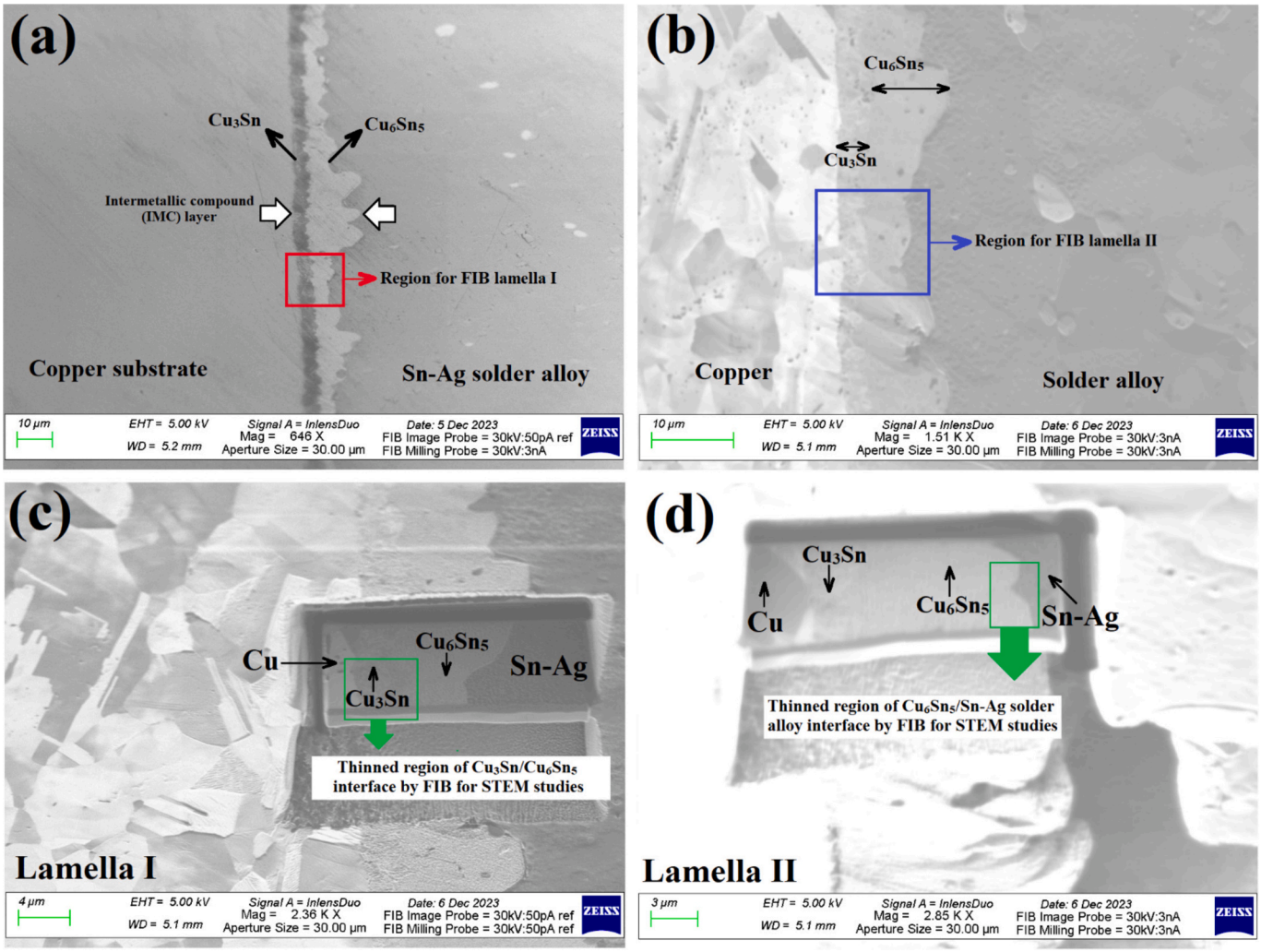


**Fig. 7.** (a) The back-scattered electrons FE-SEM image showing the cross-section microstructure of hybrid solder joint with ~2 *wt*% of reactive Fe-NPs after long times aging at the temperature of 180 °C utilized for FIB lamellas sample preparation. (b) Channeling contrast grain structures by FE-SEM imaging regarding the Cu-substrate, Sn—Ag solder alloy, $Cu_3Sn$, and $Cu_6Sn_5$ IMC layers. The FIB lamellas sample preparation from the IMC layer; (c) lamella I and (d) lamella II, with a particular focus on the thinning of (c) $Cu_3Sn/Cu_6Sn_5$ and (d) $Cu_6Sn_5$/solder interfaces.

### *3.2. IMC growth kinetics by incorporation of Fe-nanoparticles and aging treatment*

Fig. 4 represents the layer thickness measurements for $Cu_6Sn_5$, $Cu_3Sn$, and total ($Cu_3Sn$, $Cu_6Sn_5$) compounds after isothermal aging at 120 °C (a) and 180 °C (b) for Cu/Ag3.5Sn/Cu hybrid solder joints with different Fe-NP additions. The non-uniform scalloped shape of the $Cu_6Sn_5$ layer resulted to a rather high variation in thickness along the interface. As already evident from the microscopic analysis, the reaction-controlled IMC growth during the reflow process resulted in formation of both IMCs at the interface prior to aging. The diagrams in Fig. 4a and b indicate that in all cases both phases grow simultaneously with increasing the aging time, however with different growth rate. Based on the statistical data reported in Fig. 4 for the growth of the IMC layer across the solder joint at different aging temperatures for various holding times under the impact of different Fe-NPs contents (0 to 2.0 *wt* %), the general trend displays slight thickening by aging time and severe thickening of IMC layers by increasing aging temperature. Also, by increasing the fraction of Fe-NPs at the interface, the IMC layer thickness is typically decreased, as expected and explained due to the hindering role of nanoparticles (the main subject of the present research study). However, some fluctuations in IMC layer thickness variation *versus* increasing the aging time were observed, which could be commonly attributed to the slow kinetics of IMC layer growth by increasing the holding time, particularly at the preserved lower temperatures (room ambient and 120 °C).

Comparison of the measured IMC thicknesses for the solder joints after reflowing (4a, 4b at 0 h) indicates that addition of more than 1% Fe-NP results in a reduced growth of $Cu_6Sn_5$, while the very narrow $Cu_3Sn$ of about 300 nm which has been already formed at the interface during the reflow seems to be unaffected. Thermal storage at up to 480 h at 120 °C data leads only to a moderate increase in the total IMC layer thickness for all solder joints. The thickness of $Cu_3Sn$, which is in the range of 1 μm after 480 h, indicates a much faster growth than the $Cu_6Sn_5$ phase. Comparing the total IMC thicknesses of about 5.5 μm and ~ 4 μm for 0% and 2% Fe-NPs indicates a reduction of 30% upon nanoparticle additions. At the elevated aging temperature of 180 °C, a significant impact of holding time from 0 up to 480 h is observed leading to an extensive solid-state growth of both IMC layers. Previous studies on the solid-state reactions at the Cu/Sn interface suggest that at lower temperatures, the interstitial diffusion of Cu appears to be the dominant mechanism for the growth of $Cu_3Sn$ which forms at the expense of the $Cu_6Sn_5$ phase. At temperatures above 150 °C, the growth of the $Cu_3Sn$ phase has been related to the vacancy diffusion of Sn through the η phase at elevated temperatures and the subsequent reaction with the Cu substrate [40]. The growth rate of the $Cu_3Sn$ phase at 180 °C, is

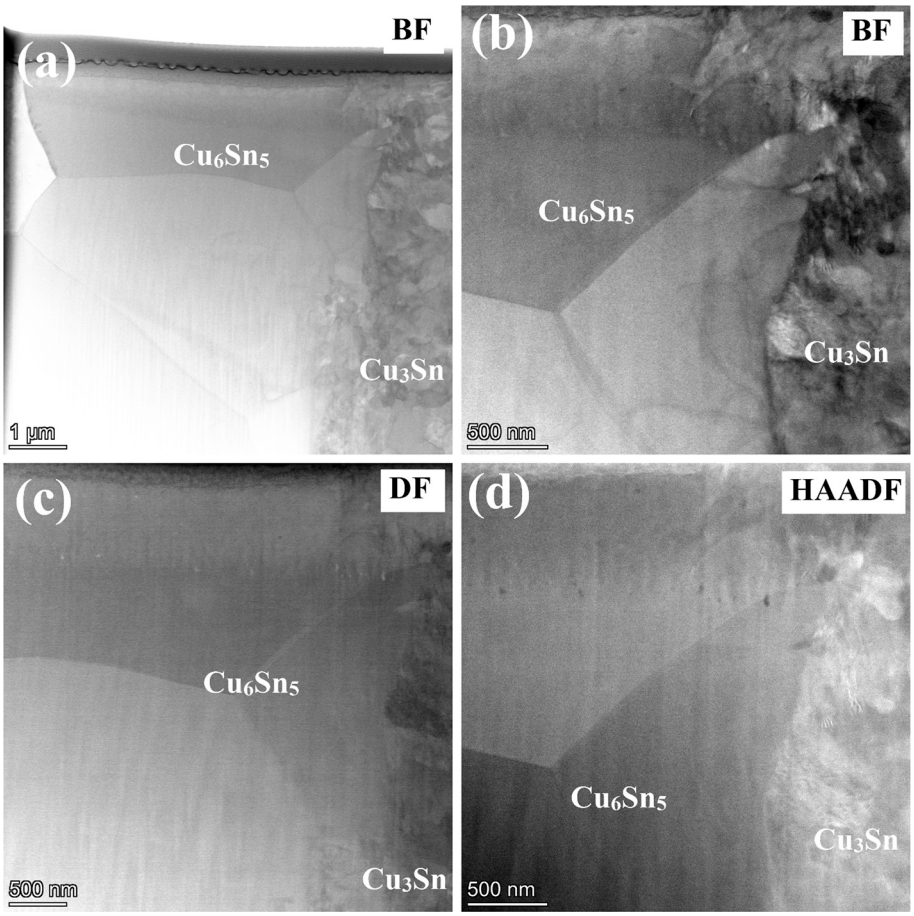


**Fig. 8.** STEM microstructures for the lamella I from the interface of $Cu_3Sn$ and $Cu_6Sn_5$ IMC layers: (a, b) BF, (c) DF, and (d) HAADF contrast images showing the sub-grains structure of these layers.

considerably higher than $Cu_6Sn_5$ with the proportion of $\varepsilon/\eta$ phases increasing from ~0.1 in the as-reflowed condition up to about 0.9 after aging at 180 °C for 480 h. Here again, higher additions of Fe-NP resulted in a reduction of up to 20% in the total IMC layer thickness (Fig. 4b).

In Fig. 4b, the thickness of the IMC layer with 0.5 *wt*% Fe-NP is the highest in the first four aging times. Besides, the thickness is lower than the original, as the aging time has reached 480 h. According to the observations, under such low content of Fe-NPs, they can probably be almost diffused through the structure of IMC layers with less hindering role against their propagation (as will support with the subsequent electron microscopy studies) in the form of nano-scale precipitates or inclusions. Such an effect becomes evident at the elevated aging temperature. Still, the fluctuation of data and error bars in the various IMC thickness layer calculations requires attention, in addition to the probable mechanism described at the structural level.

The growth kinetics of the IMC layers was evaluated by Eq. (1) assuming a diffusion-controlled growth at both annealing temperatures;

$$d = k\sqrt{t} \tag{1}$$

where $d$ is the layer thickness, $k$ is the reaction rate constant, and $t$ is the aging time. The plots of IMC thickness ($d$) as a function of square root of aging time ($t^{0.5}$) for the Fe-NP hybrid joints are presented in Fig. 5a and b. The plots which follow an almost linear relationship are in conformity with diffusion-controlled growth mechanism in the entire temperature range for all samples. The variation of the reaction rates of the two IMC layers with increasing the Fe-NP content of the joints at two different aging temperatures are shown in Fig. 6a and b. The plots show a clear reduction of reaction rates for total ($Cu_3Sn$, $Cu_6Sn_5$) IMCs upon Fe-NP additions at both temperatures with a considerable total reduced growth rate of up to 40% for the highest amount of nanoparticle additions. Furthermore, at an aging temperature of 120 °C and up to 1 *wt*% of Fe-NPs addition, the Sn-rich $Cu_6Sn_5$ phase grows dominantly, except of the joints with 2 *wt*% of Fe-NPs which show an opposite trend (Fig. 6a). By increasing the temperature to 180 °C, the reaction rates of the both phases are reversed resulting a significant increase in the growth rate of the Cu-rich phase by a factor of two (Fig. 6b). To summarize, at lower temperatures the growth kinetics of the total IMC layers is dominated by the $Cu_6Sn_5$ compound, where at elevated temperatures the $Cu_3Sn$ remarkably contributes to the total IMC layer thickness.

### 3.3. Activation energy for the diffusive growth kinetics of IMC layers

The activation energy ($Q$) for the IMC growth in the solid-state reaction was estimated by plotting $ln(k)$ as a function of $1/T$ and determining the slope of a linear fit based on the Arrhenius equation (Eq. 2):

$$k = k_0 exp\left(-\frac{Q}{RT}\right) \tag{2}$$

with $k_0$ being the frequency factor; $R$, the gas constant (~8.314 J/mol.K) and $T$, the absolute temperature in Kelvin. The $k$ values were obtained from the fits for IMC growth rates at 353 and 453 K in Figs. 5a, b. The calculated activation energies and reaction rates (efficient diffusion coefficients) for $Cu_3Sn$, $Cu_6Sn_5$, and total ($Cu_3Sn$, $Cu_6Sn_5$) growth at the Ag3.5Sn/Cu interface with different amounts of Fe-NPs are given in Fig. 6c and Table 2. Generally, the derived activation energies for the formation of total ($Cu_3Sn$, $Cu_6Sn_5$) increase with the higher amounts of

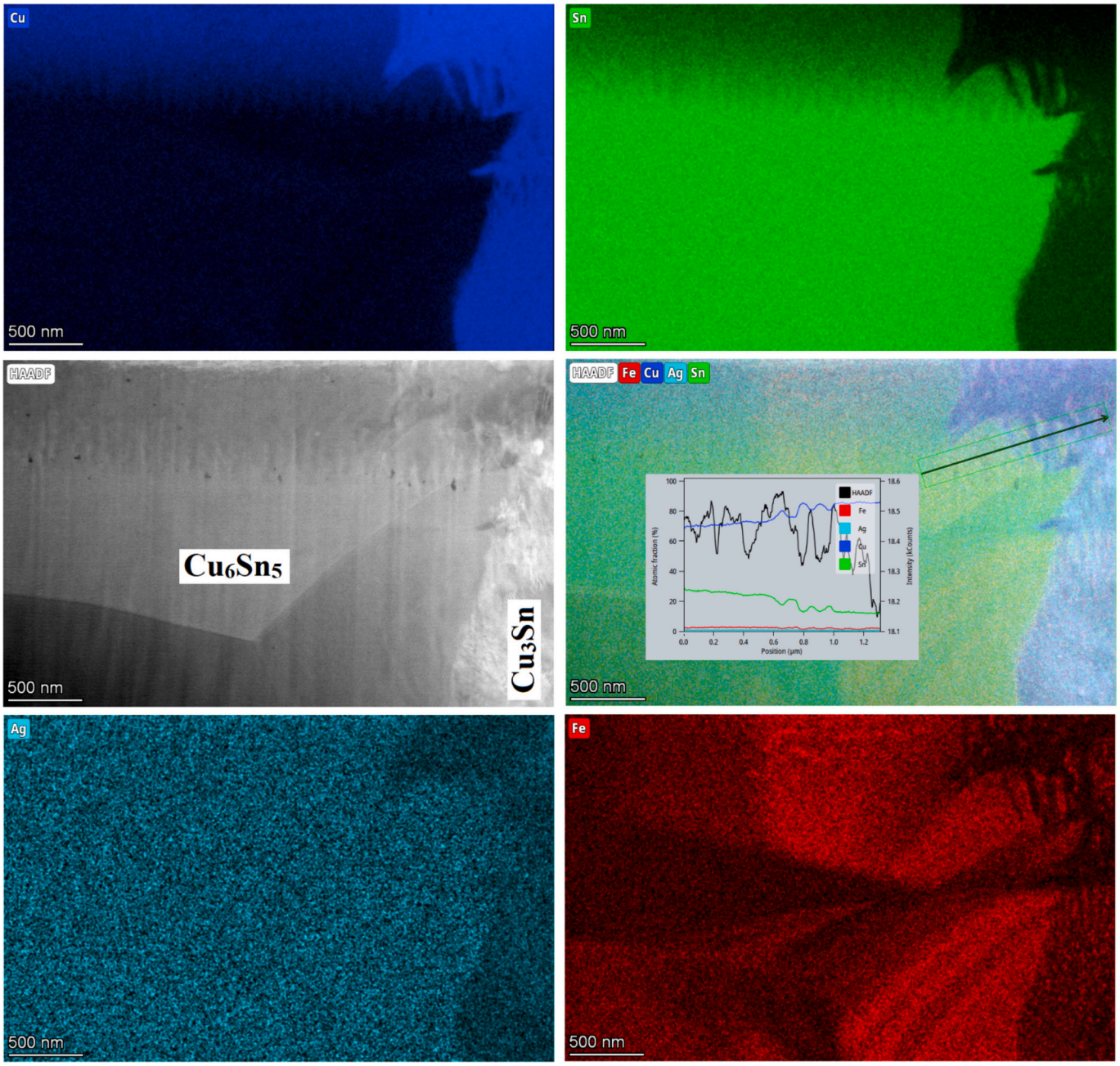


**Fig. 9.** The bright field STEM image along the corresponding EDS maps for the distribution of Cu, Sn, Ag, and Fe elements, as combined with a line-scan analysis from the $Cu_6Sn_5/Cu_3Sn$ interface, showing the diffusion of the iron element in the head of the $Cu_3Sn$ layer formation.

Fe-NPs, confirming their positive impact on hindering the total IMC growth in the hybrid solder joints. Moreover, it can be clearly seen that upon addition of up to 1 *wt%* Fe-NPs, the activation energy of the $Cu_3Sn$ increases steadily and is almost 2-fold of that obtained for $Cu_6Sn_5$. Increasing the amounts of NPs to 2 *wt%* results in a decrease of *Q* for $Cu_3Sn$ with a simultaneous increase of that for $Cu_6Sn_5$ (Fig. 6c), indicating a change in the growth mechanisms of both IMCs in the presence of higher amounts of Fe-nanoparticles and Fe containing reaction products.

The solid-state growth kinetics of the $Cu_3Sn$, $Cu_6Sn_5$ in Sn/Cu diffusion couples, and Sn-based solder alloys on Cu substrates have been intensively studied with a broad range of activation energies for the formation of the two intermetallic phases as well documented in several review articles [41–44]. Table 3 provides a comparison of our results with the activation energies reported in the literature for Cu—Sn intermetallic compounds in Sn-based solders with or without additional elements. The reported values are in a wide range depending on the Sn content in the solder, the characteristics of the Cu substrate, the presence of impurities or alloying elements, and the applied aging temperature and time range. The values for $Cu_3Sn$ and $Cu_6Sn_5$ are reported to be, *e.g.*, 38.7 and 47.3 kJ/mol in $Cu/Cu_3Sn/Cu_6Sn_5/Sn$ diffusion couple [45] up to values in the range of 115 and 58 kJ/mol in SAC305/Cu solder joints for both IMCs respectively [19,46]. The lower activation energy reported for $Cu_6Sn_5$, which conforms with our results, is explained by the lower stability of this phase and its accelerated mechanism of formation. The growth mechanism of interfacial IMCs in SAC + X solder joints with minor additions Ni, Co, and Fe has been explained by partial substitution of Cu atoms in the IMC layers. This results in a reduction in the interdiffusion of Sn atoms due to an increased lattice strain, which is induced by the atomic radius mismatch between Cu and the additional element.

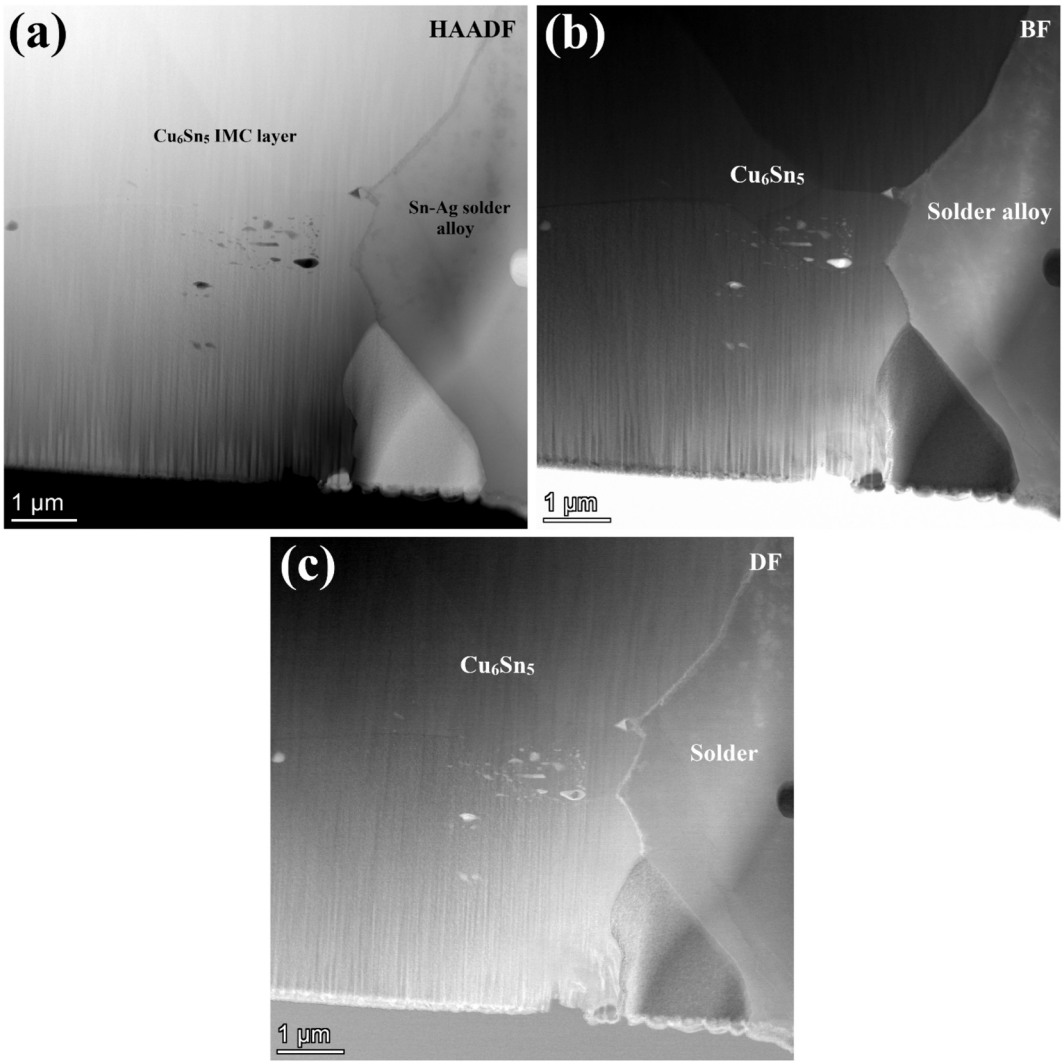


**Fig. 10.** The general STEM views for the nano-scale structure of lamella II from the interface of $Cu_6Sn_5$ IMC layer and solder alloy: (a) HAADF, (b) BF, and (c) DF imaging modes.

While neither considerable effect [29] nor a promoted growth of $Cu_6Sn_5$ was reported [47], a reduction in the thickness of $Cu_3Sn$ was achieved, which is in line with the higher activation energy of this phase. For solder joints produced with a Fe-modified SAC alloy, the increased reliability was associated with the enrichment of the entire IMC layer with Fe, with the highest concentrations being in the $Cu_6Sn_5$ layer near the $Cu_3Sn$ interface. The dissolved Fe atoms seemed to slow down the interfacial inter-diffusion process and minimize the Kirkendall voiding at the $Cu_3Sn$/Cu interface, thus hindering the embrittlement of the joint after long-term aging [27].

The body of research concerning the growth kinetics of composite solder joints incorporating reactive metallic nanoparticles predominantly focuses on joints augmented with Ni and Co, with comparatively limited attention directed toward the effects of Fe nanoparticles. Existing studies indicate that the addition of Ni and Co nanoparticles, elements exhibiting significant solubility in intermetallic compound (IMC) layers, leads to the formation of $(Cu, Co)_6Sn_5$ and $(Cu, Ni)_6Sn_5$ phases, akin to an alloying effect. Investigations into the growth kinetics of SAC/Cu solder joints augmented with Ni-doped flux have revealed an accelerated growth rate of the thermodynamically more stable Sn-rich phase alongside a concomitant deceleration in the growth rate of $Cu_3Sn$. Compared to non-doped alloys, these phenomena culminate in reduced activation energies for the total IMC layer and the Sn-rich phase (η), measured at 48 and 43 kJ/mol, respectively, upon aging up to 175 °C. Conversely, the activation energy for the formation of $Cu_3Sn$ (ε) increases from 81 to 96 kJ/mol under similar aging conditions.

The advantageous influence of Ni nanoparticle additions is attributed to the planar morphology of the resulting $Cu_6Sn_5$ layer, alongside the stabilization of its hexagonal structure and the concurrent suppression of $Cu_3Sn$ layer growth. However, the specific role of Fe nanoparticles in impeding the growth kinetics of $Cu_6Sn_5$ and $Cu_3Sn$ phases is intricately linked to the distribution of Fe and the ensuing interfacial reactions, elucidated through high-resolution microstructural investigations in subsequent sections [48]. These investigations are poised to provide valuable insights into the mechanistic underpinnings governing the interaction between Fe nanoparticles and solder matrix constituents, thereby enriching our understanding of the complex dynamics governing composite solder joint formation and evolution. As calculated and expressed in Table 3, by increasing the fraction of incorporated reactive Fe-NPs from ~0 up to ~2.0 *wt*%, the activation energy of formation regarding both $Cu_3Sn$ and $Cu_6Sn_5$ IMC layers is continuously elevated, which can support the impressive hindering contribution of these secondary phase reactive agents against coarsening of IMC layers by annealing temperature and aging time.

### 3.4. FIB/STEM analysis of the hybrid solder joint IMC interfaces

In Fig. 7a, the backscattered electron contrast of FE-SEM microscopy

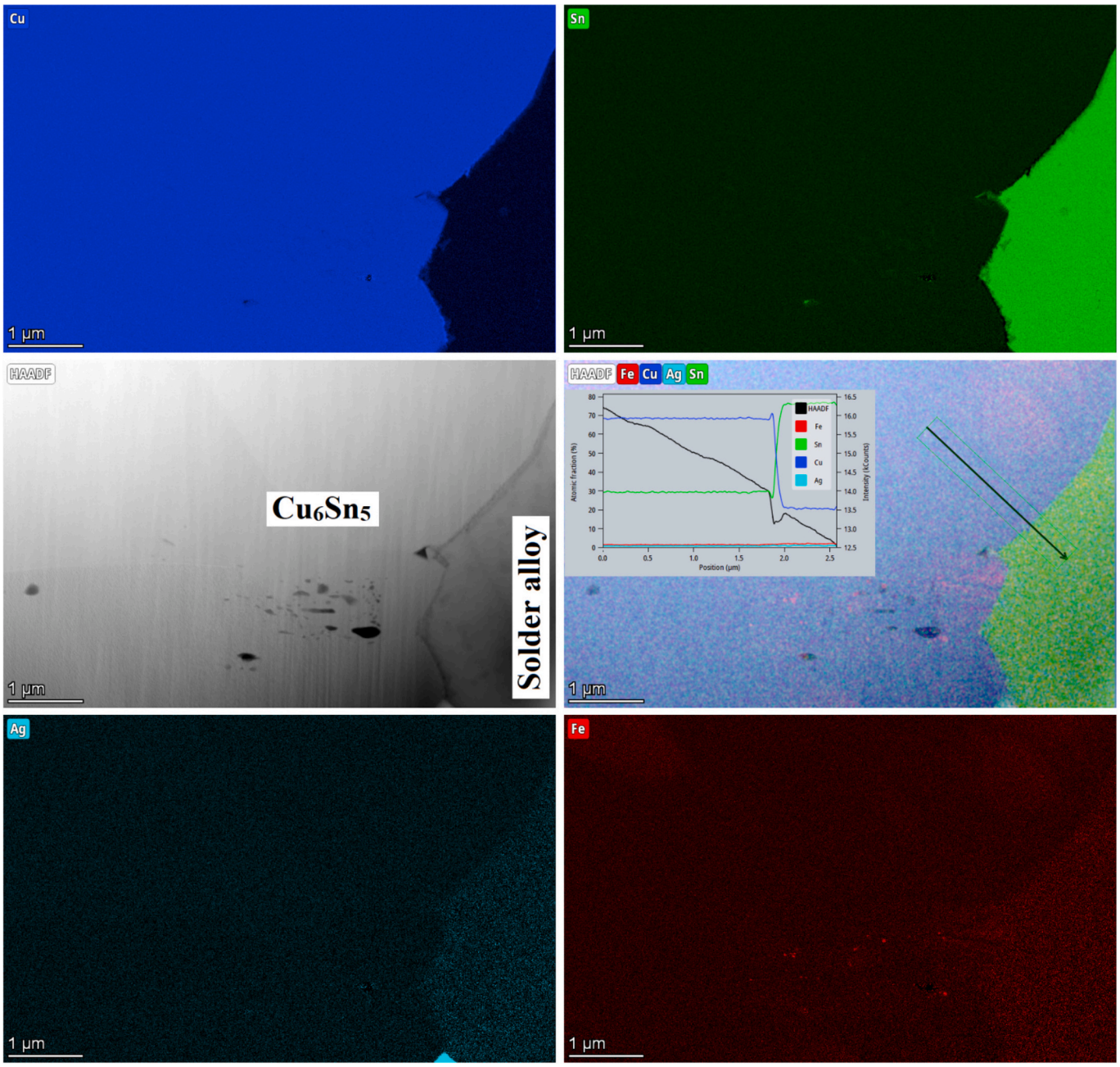


**Fig. 11.** Low-magnification STEM/EDS elemental map from the interface of $Cu_6Sn_5$ IMC layer with the Sn—Ag solder alloy.

images obviously demonstrates two distinguished IMC layers of $Cu_3Sn$ and $Cu_6Sn_5$ across the interface of the hybrid solder joint with ~2 *wt*% of Fe-NPs after long-time aging treatment at the elevated temperature of 180 °C. The location for the preparation of the first lamella by FIB across the solder joint is also indicated. Fig. 7b shows the channeling contrast from the grain structure for IMC layers, copper substrate, and solder alloy, along with the region of interest for the second FIB lamella.

The FE-SEM microscopy images depicted in Fig. 7c and d illustrate the extraction and thinning steps conducted on the first and second FIB samples, designated as lamella I and II, respectively. In both cases, meticulous efforts were made to encompass all components of the solder joint interface—namely, the Cu-substrate, solder alloy, and both $Cu_3Sn$ and $Cu_6Sn_5$ intermetallic compound (IMC) layers—within the FIB lamellas. However, to mitigate potential distortion damage during the FIB thinning process, particular emphasis was placed on further reducing the thickness of the $Cu_3Sn/Cu_6Sn_5$ and $Cu_6Sn_5$/solder alloy interfaces during the final thinning procedure for lamellas I and II, respectively.

Subsequently, the STEM microstructures and corresponding EDS elemental maps pertaining to the first scenario of lamella I, focusing on the interface between the $Cu_3Sn$ and $Cu_6Sn_5$ IMC layers, are presented in Figs. 8 and 9. Notably, in consistent alignment with the channeling contrast microstructures, the grain structure of the $Cu_3Sn$ IMC layer exhibits a significantly finer morphology compared to that of $Cu_6Sn_5$. Furthermore, the FE-SEM/EDS elemental maps depicted in Fig. 9 delineate the diffusion and enrichment of iron elements both in front of the $Cu_3Sn$ layer and throughout the structure of the $Cu_6Sn_5$ compound following reflow solidification and subsequent thermal aging treatments. These comprehensive analyses provide valuable insights into the microstructural evolution and elemental distribution across the solder joint interface, facilitating a deeper understanding of the underlying mechanisms governing interfacial interactions and phase transformations within composite solder joints. This matter could be an

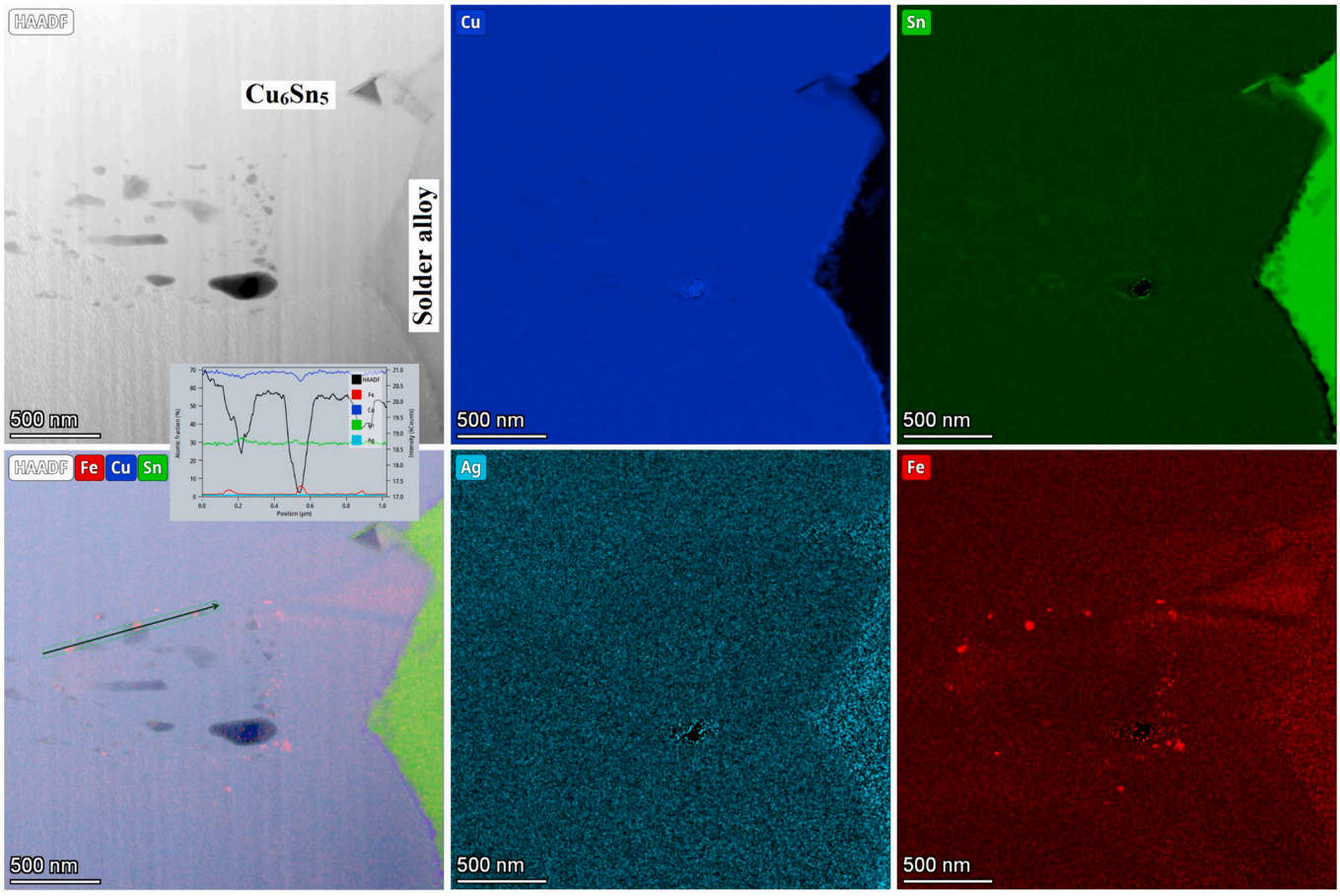


**Fig. 12.** A higher-magnification STEM/EDS analysis results from the nano-scale features inside the leading edge of $Cu_6Sn_5$ IMC layer and also in the front of that within the solder alloy matrix, while the line scale profile and distribution map demonstrate the *in situ* reaction and segregation of Fe element, accordingly.

indicator regarding the formation of a thin diffused $(Cu, Fe)_6Sn_5$ layer at the interface of two IMCs of $Cu_3Sn$ and $Cu_6Sn_5$, while the interrelated reports on other systems in the literature [6] to this context indicate the formation of semi-compounds of reaction-formed intermetallics such as $(Cu, Ni)_6Sn_5$. On the other side, the interface between the leading $Cu_6Sn_5$ IMC layer and solder alloy was studied using lamella II, while the resultant general view STEM microstructures are demonstrated in Fig. 10. In these HAADF, BF and DF microstructures, the left side corresponds to the $Cu_6Sn_5$ IMC layer with dispersed reinforcing agents in the middle, and the right side of lamella demonstrate solder alloy head of that. The low-magnification STEM/EDS mapping of Fig. 11 exhibits the elemental distribution across the interface between $Cu_6Sn_5$ IMC and solder alloy. Regarding such a broad field of elemental analysis across the interface, some segregated sites for iron clustering inside the $Cu_6Sn_5$ part, as well as higher concentrations of Fe in front of this layer through the solder alloy region, are observed. However, the case of EDS analysis from the interface region with more intense elemental segregation at higher magnification, as displayed in Fig. 12, reveals the iron segregation and its *in situ* chemical reactions with the tin solder alloy through the IMC structure of $Cu_6Sn_5$, along with Fe elemental ejection in front of the solidification edge inside the solder alloy. Such the STEM characterizations for the $Cu_6Sn_5$/Sn-Ag interface across the hybrid joint, as shown in Figs. 10 to 12 depict the occurrence of nano-scale precipitation for both sides of the intermetallic part and the solder alloy which requires more advanced studies. In this context, the high-magnification HAADF, BF, and DF STEM results from the distributed nano-scale features within the $Cu_6Sn_5$ compound structure are analyzed in Fig. 13. In the HAADF contrast graphs, the black region of particles demonstrates the non-reacted or semi-reacted regions, and also the graded grey contrast boards reveal the new *in situ* formed compositional phases. Such trends of chemistry color profiles in the BF and DF contrast STEM pictures are *vice versa*. Furthermore, Fig. 14 exhibits such the nano-scale features segregated in the line of solidification interface and also in front of that through the solder alloy matrix, which illustrate a uniform segregation of nano-metric iron along the edge besides subsequent nano-scale precipitation of iron-rich compounds through the reflow solidified solder.

### 3.5. *The nano-scale mechanistic model enrolling the contribution of reactive Fe-NPs*

The mechanisms for the formation of the IMC layers across the solder joints and their subsequent thickening growth were often reported in the literature and can be summarized as a large dependency of the reliability of solder joints on the formation of reaction layers at the interface during the early stages of reflow solidification, which can significantly influence the further IMC layer development [52]. Undergoing the reflow of Cu/Sn-Ag lead-free solder joint, as worked on the present research, two well-recognized IMC layers of $Cu_6Sn_5$ and $Cu_3Sn$ were formed across the interface by a particular sequence of η-phase precipitation at the Cu/Sn interface followed with the incubated ε-phase precipitation across the $Cu_6Sn_5$/Cu interface [14]. The higher thermodynamic driving force governing the precipitation of the $Cu_6Sn_5$ phase, coupled with the rapid atomic jumping kinetics and disparities in interfacial energies, underpin the observed precipitation sequence at the metastable interface of the solder joint. Realistic observations indicate that upon initiation of reflow solidification, the exceedingly swift kinetics of $Cu_6Sn_5$ phase enable its immediate nucleation at the solid/liquid interface, swiftly growing

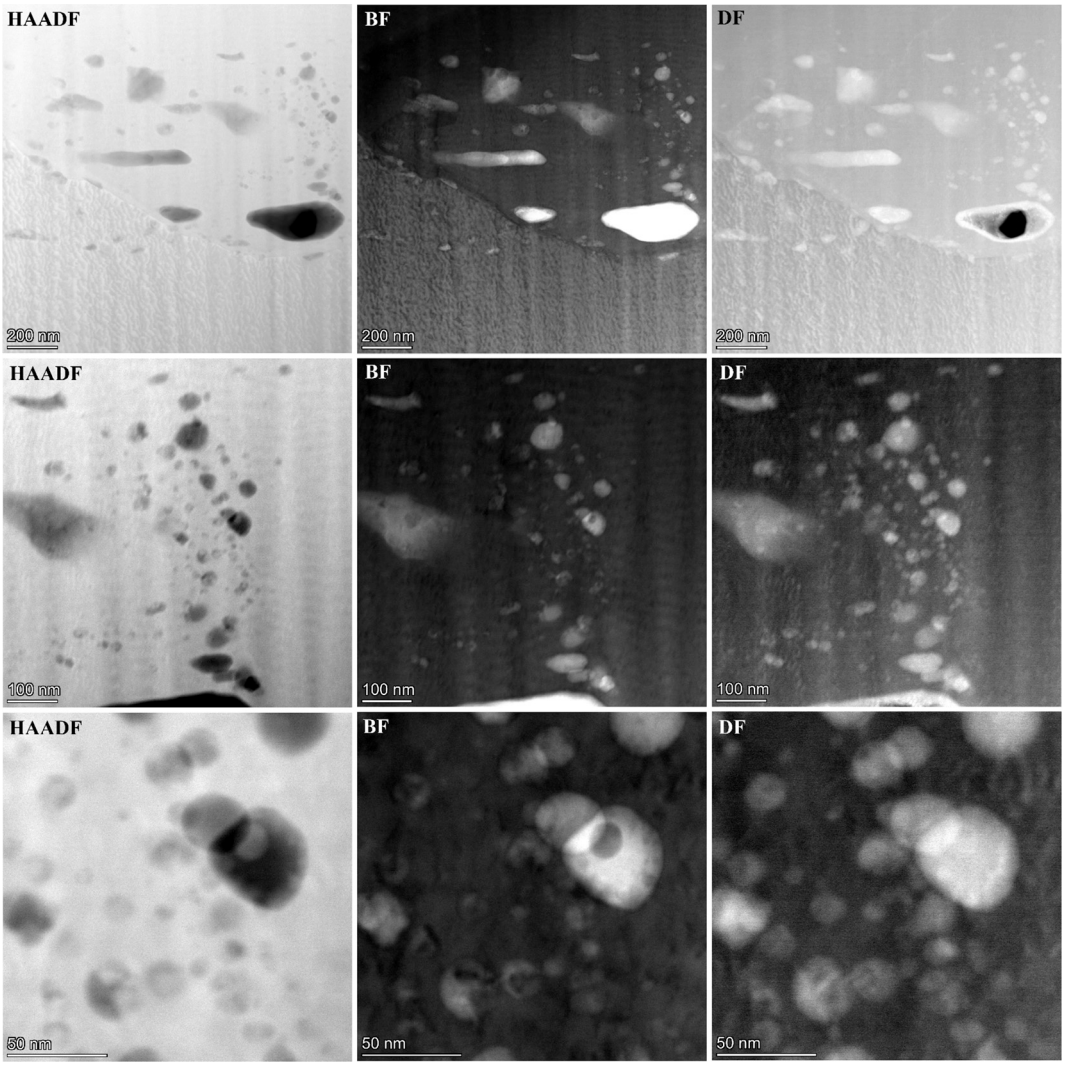


**Fig. 13.** High-magnification HAADF, BF, and DF STEM images from the distribution of nano-scale precipitates (semi-reacted elongated Fe and *in situ* formed $FeSn_2$ round phase) through the matrix of $Cu_6Sn_5$ IMC layer.

under the influence of mass transport phenomena to establish a contiguous layer of intermetallic compound (IMC) at the interface with Cu, occurring within a fraction of a second [53,54]. Subsequently, the diffusion of Cu from the substrate emerges as the pivotal controlling mechanism governing the coarsening of this η-phase layer. Notably, the substantial dependency of diffusion mass flow on the energy of grain boundaries within this solidified $Cu_6Sn_5$ layer can induce a characteristic morphology resembling scallop-like features, contributing to its thickening over time. On the other side, the incubation time for the formation and growth of the $Cu_3Sn$ IMC layer is quite high, and such feeble kinetics renders it difficult to characterize the nucleation of the ε phase during the earlier stages of soldering. However, the corresponding few investigations revealed the columnar lateral growth of this ε phase by thermal aging, with a more refined grain structure, as also detected in the current work by channeling contrast imaging microstructures of Figs. 2 and 3. In this context, phase-field modeling is a very powerful simulation technique for the prediction of IMC layer formation at the interface during reflow solidification and their consequent coarsening by thermal aging along with predicting the microstructural evolutions, also considering the impact role of solder alloy composition and atomic diffusion varying by processing temperature, as well as the solute-trapping mechanisms [16].

As emphasized earlier, the focus of the present research is to study the concurrent interaction between the application of reactive Fe-nanoparticles at the interface of solder joint with these described mechanisms for the formation of two $Cu_6Sn_5$ and $Cu_3Sn$ IMC layers and, accordingly, in-depth characterization of the involved nano-scale mechanisms behind the suppressing role of Fe-NPs. To the end of such an almost diffusion-based majority competition, considering the presented FIB/STEM microstructures from different regions of the interface in Figs. 7–14, a mechanistic model regarding the impact of reactive Fe-NPs at the interface of the solder joint and contributed nano-scale mechanisms, as demonstrated in the schematic plots of Fig. 15, can be proposed. Fig. 15a illustrates the schematic demonstration regarding the pre-placement of Fe-NPs doped flux at the interface of solder alloy and copper substrate (although on both sides, only one of them) before placing in the atmosphere-controlled furnace and running the primary heat treatment cycles. In Fig. 15b, the cluttering of Fe-NPs, their trapping inside the structure of the $Cu_6Sn_5$ IMC layer, and partially interfacial chemical reactions to form the $FeSn_2$ phase as surrounded by the Fe-clusters during reflow solidification at the interface are demonstrated. Besides, segregating the remaining Fe-NPs and their clusters in front of the solidification edge as accumulated by the migration of the $Cu_6Sn_5$ boundary toward the solder alloy matrix is addressed.

In Fig. 15c, upon age heat treatment by placing such a designed hybrid solder joints at elevated temperatures (120 and 180 °C) and holding it for long-times (up to 480 h), undergoing the solid-state elemental diffusion-based mechanisms, three competitive mechanistic

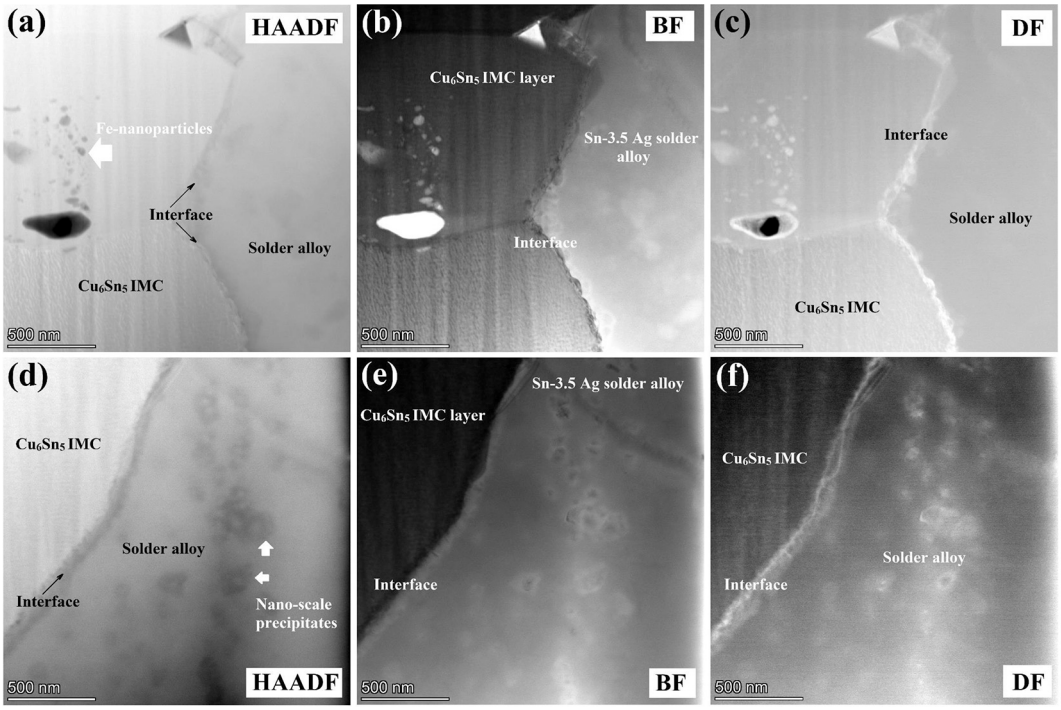


**Fig. 14.** The STEM images from (a-c) the interface of $Cu_6Sn_5$ layer and solder alloy and (d-f) dispersed nano-scale precipitates through the matrix of solder alloy at high magnifications under different microstructural contrasts of (a, b) HAADF, (b, e) BF, and (c, f) DF modes.

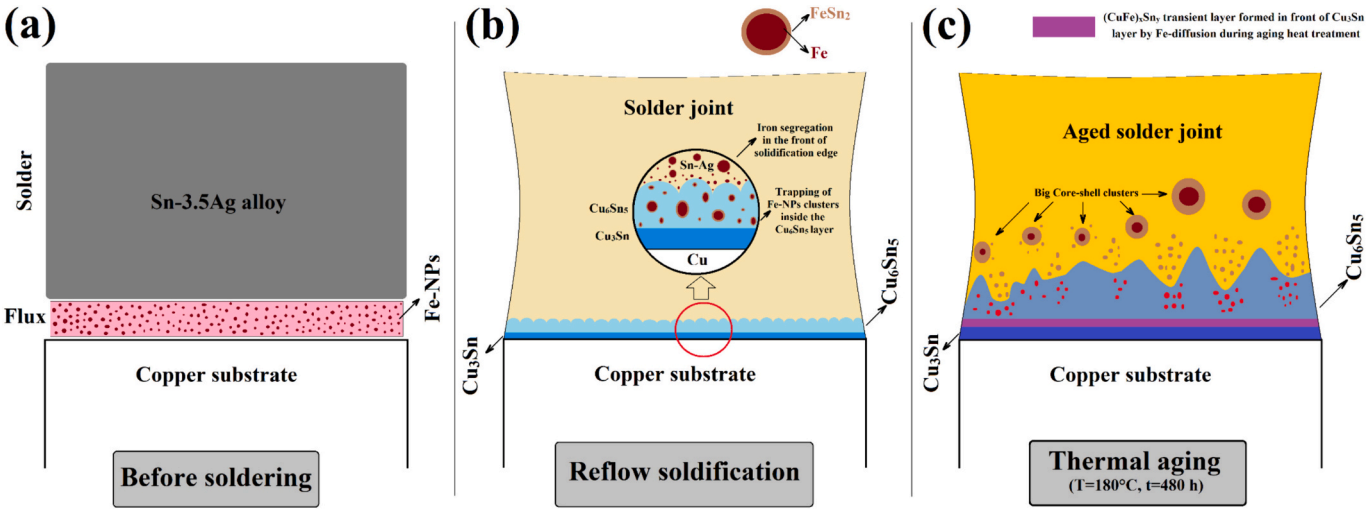


**Fig. 15.** Schematic of the nanoscale mechanistic model representing the credible mechanisms for the formation of a sustainable microstructure during reactive hybrid soldering: (a) Joint design before soldering, (b) reflow solidification, and (c) thermal aging treatment.

interactions can be activated; (*i*) high chemical potential for diffusive progression growth of $Cu_3Sn$ and $Cu_6Sn_5$ IMC layers toward the solder alloy matrix, (*ii*) significant tendency of iron nanoparticles for chemical reaction with tin and formation of $FeSn_2$ phase and coarsening toward the state of higher stability according to the diffusive interfacial solid-state chemical reactions, and (*iii*) kinetically hindering role of Fe nanoparticles, their clusters, and corresponding *in situ* reacting products against the growth of $Cu_3Sn$ and $Cu_6Sn_5$ phases and migration of their interfaces.

Indeed, thermodynamic calculations based on equilibrium states allow for the prediction of the fate of the introduced Fe-NPs, which are anticipated to undergo consumption and integration into two distinct reaction and diffusion zones during various stages of reflow solidification and subsequent thermal aging [6]. Notably, a diffusion layer forms for iron in front of the $Cu_3Sn$ layer, precipitating structural changes within the $Cu_6Sn_5$ intermetallic compound (IMC) toward the formation of a complex compound denoted as $(Cu, Fe)_xSn_y$. This compound, with a probable stoichiometry of $(Cu, Fe)_6Sn_5$, acts as a reaction layer formed post-reflow and discerned through STEM/EDS analysis, significantly impeding further growth of IMCs during subsequent aging modifications.

Within the framework of thermodynamic stability, alterations in the formation energy ($\Delta E_f$) resulting from the substitution of Fe atoms within the structure of the η-$Cu_6Sn_5$ crystal lattice and the stabilization of a new stoichiometry ($Cu_{24-x}Fe_xSn_{20}$) can be estimated utilizing the following expression [55]:

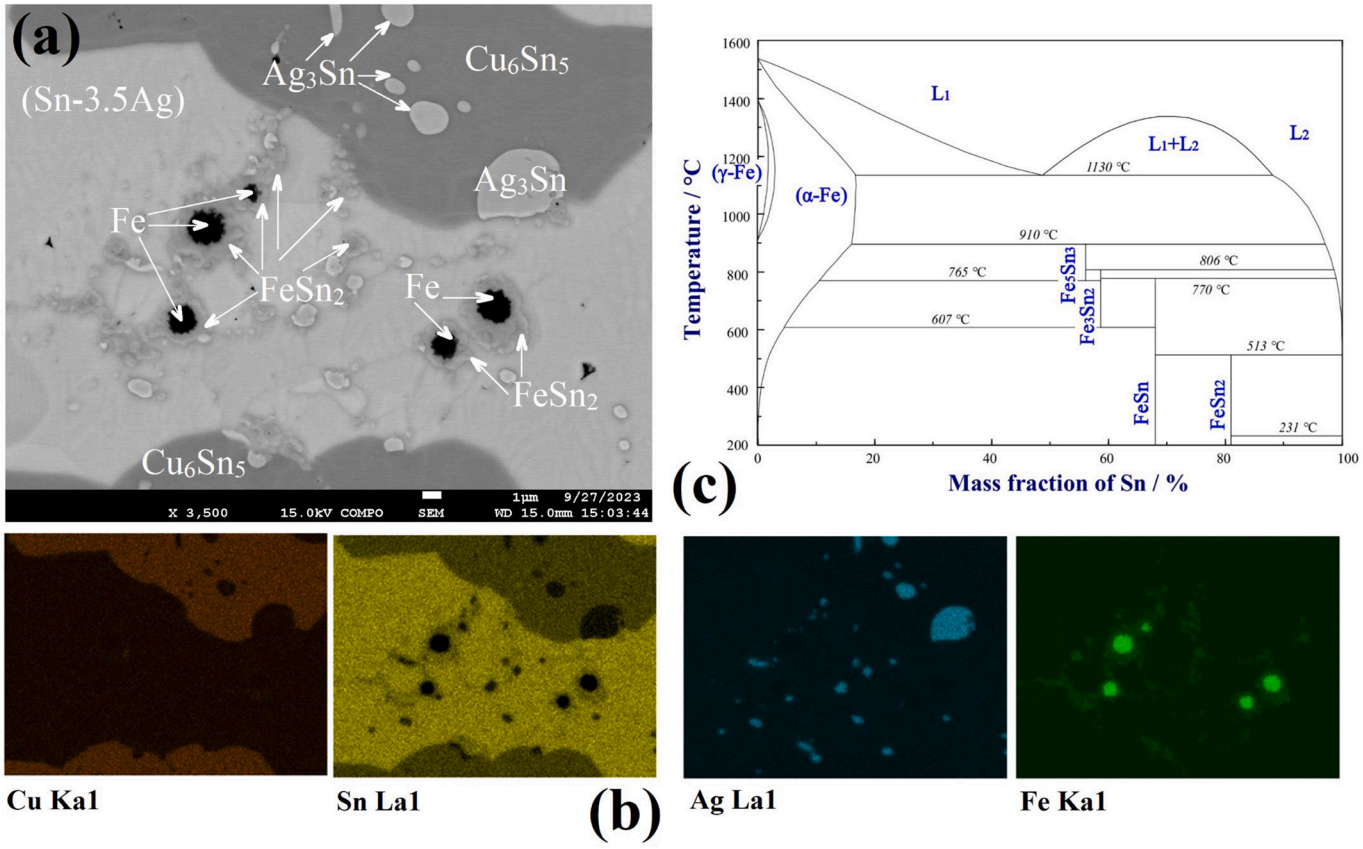


**Fig. 16.** *In situ* chemical reactions between iron particles and Sn—Ag solder alloy after reflow solidification and thermal aging, as characterized by (a) FE-SEM microstructural imaging and (b) elemental EDS mapping, based on (c) the equilibrium thermodynamic phase diagram of Fe—Sn system [56].

$$\Delta E_f = \frac{1}{44}\left(E[Cu_{24-x}Fe_xSn_{20}] + xE[Cu] - 4E[Cu_6Sn_5] - xE[Fe]\right) \quad (3)$$

while $x$ is varied with the integer values of 0, 1, 2, 3, 4, *etc.* Although, more discussion regarding the formation mechanism and growth kinetics of diffused (Cu, Fe)$_6$Sn$_5$ layer is inconclusive, as further characterization studies by advanced techniques such as atom probe tomography (APT) would be required. Also, the variation of the thickness of the $Cu_6Sn_5$ IMC layer with a morphology of known as scallop is strongly correlated with the population and distribution of Fe-NPs and clusters inside this layer and in front of that at different locations.

The FE-SEM microstructural image and EDS elemental mapping analysis results regarding the reflowed/aged hybrid solder joint as depicted in Fig. 16a and b, respectively, can consistently validate the above proposed mechanistic model (as also schematically illustrated in Fig. 15) for the contribution of iron particles upon reflow soldering and thermal aging, according to the binary phase diagram of Fig. 16c between elements of Fe and Sn, while determined by the equilibrium thermodynamic calculations [56]. As shown in Fig. 16a, the clusters of iron nanoparticles segregated inside the molten solder alloy matrix, displayed by black contrast features in this FE-SEM micrograph, are continuously reacting with the Sn—Ag solder alloy to form the *in situ* products around them, addressed by grey contrast new particles while some of these agents are also separated and dispersed within the solder matrix. The EDS results of Fig. 16b, and particularly the iron element distribution map, can support the mentioned hypothesis, indicating such a depletion of Fe in some interaction regions around the clusters, while those areas are simultaneously enriched by Sn element. Analyzing the binary Fe—Sn phase diagram of Fig. 16c, several intermetallic compounds between iron and tin possess the chance of formation over different ranges of compositional stoichiometry and processing temperature. Meanwhile, for the higher fractions of Sn (as in the solder alloy) and at room temperature, the $FeSn_2$ seems the most probable and stable phase of this system. Based on the exciting observations indexed in the present work by advanced microscopy characterizations concerning previous similar attempts in the literature, several differences can be announced considering the role of reactive iron nanoparticles as doped in flux in suppressing the growth kinetics of IMC layers. According to the literature survey of this context, in most cases, the iron agent was added at the soldering interface by some pre-treatment techniques such as coatings. The subsequent reflow process resulted in the formation of a new compound layer at the interface, mostly $FeSn_2$, that can act as a barrier for the inter-diffusion of elements against the progressive creation of different compounds at the interface. In the interesting research study by Gao et al. [57], they applied a thin layer of iron-nickel by metallization on the copper substrate before soldering, which resulted in the formation of a compact $FeSn_2$ layer at the interface upon reflow solidification. Such a dense layer exhibition at the interface of the solder joint can contribute as a diffusion barrier against the formation and growth of subsequent IMC layers and even alter their compositions toward the (Ni, Cu)$_3$Sn$_4$ and (Cu, Ni)$_6$Sn$_5$ stoichiometry, with higher activation energies of formation (in the range of 86 to 97 kJ/mol). However, in this study, by applying iron as the reactive nanoparticles doped in the flux at the interface of the solder joint, a combination of variable mechanisms shown in the schematic plots of Fig. 15 can be enrolled in retarding the IMC layers formation during reflow solidification and their subsequent thickening by thermal aging treatment. As the leading objective of this research, Fe-NPs, which are introduced at the soldering interface by flux, contribute to the corresponding mechanism encountered during the liquid-solid and solid-state reactions individually and not by the formation of a continuous layer at the interface that acts as a diffusion barrier.

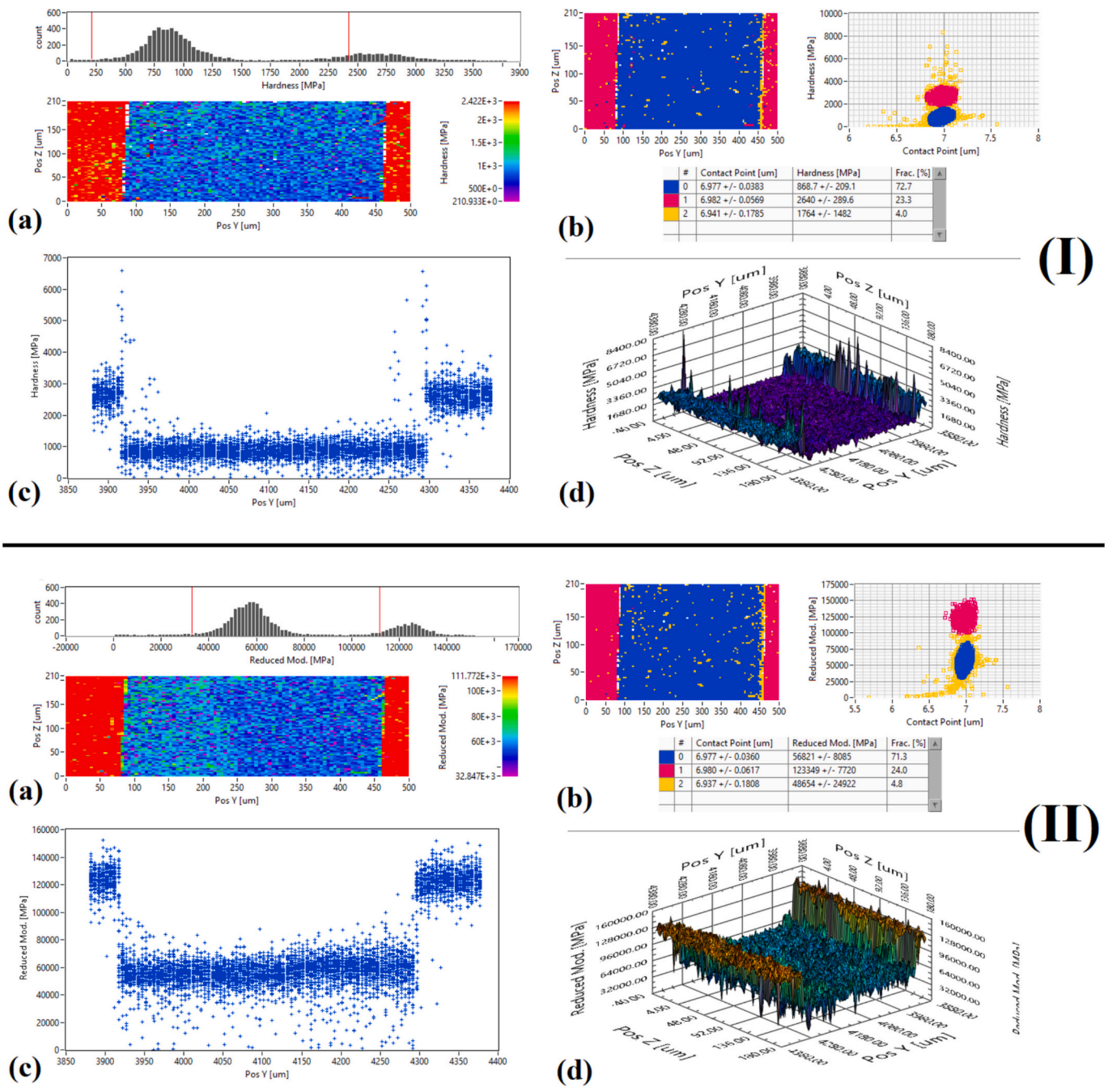


**Fig. 17.** (I) The nanoindentation hardness and (II) the calculated reduced elastic modulus parameter estimated based on material stiffness changing upon nano-indentation across the non-reinforced solder joint, no doped Fe nanoparticles: (a) Contour map, (b) data analysis/corresponding average values plus the standard deviations results, (c) 2D, and (d) 3D distribution profiles.

### *3.6. Assessment of the localized mechanical stiffness of the soldered joints*

As stated before, the mechanical function of solder joints in this research in correlation with the above-described nano-scale mechanisms around the IMC layer and its growth during reflow solidification and aging treatment was assessed in terms of localized mechanical testing across the hybrid solder joint interfaces by applying nanoindentation mapping. To cover such a crucial subject, two different solder joints of non-reinforced (0 *wt*% Fe-NPs) before aging and aged hybrid one with ~2 *wt*% Fe-NPs were considered for investigation as a means of consistent comparison and validation of the previously expressed nanoscale models. Hence, the corresponding indentation hardness and reduced modulus properties for both solder joints are presented and compared in Figs. 17 and 18. Concerning the nanoindentation results for the non-reinforced and reinforced aged solder joints, the formation of the IMC layers with a higher hardness value along both sides of the hybrid joint regarding the later scenario is revealed by hardness mapping of Fig. 18(I). However, in the case of the solder joint without the addition of iron nanoparticles, a very thin layer of IMC at the cross-section interfaces can be captured for calculations of hardness and reduced modulus upon nanoindentation mapping, as shown in Figs. 17 (I) and (II), respectively. Accordingly, in some points across both sides of the interfaces of the solder joint, the hardness values were found to be as high as 6000 to 7000 MPa, compared to the average calculated data of ~869 and 2640 MPa for the solder alloy matrix and copper substrate, respectively. However, based on the hardness contour map of Fig. 17(I)

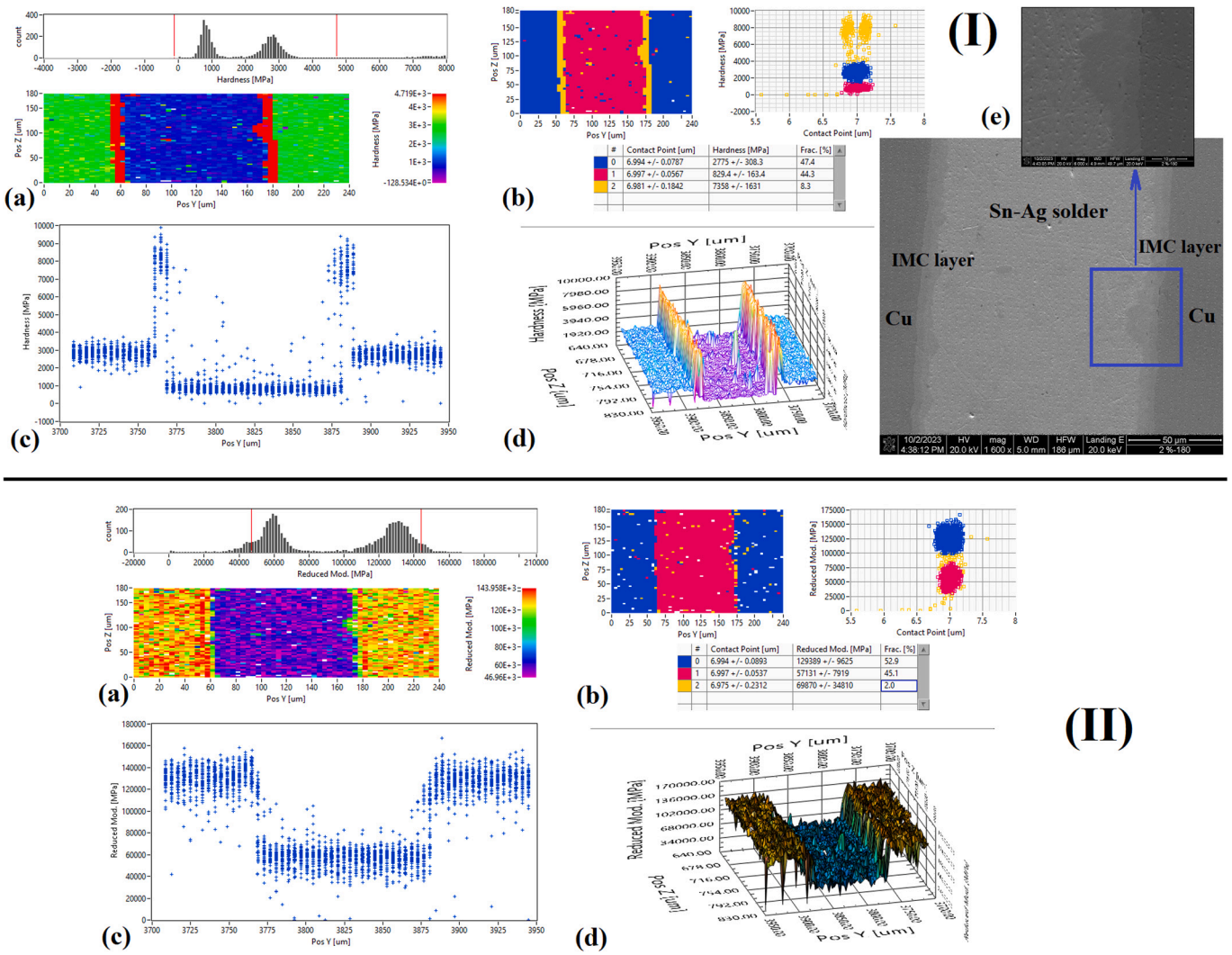


**Fig. 18.** The analyzed results for (I) hardness and (II) reduced elastic modulus based on the nanoindentation testing across the aged hybrid solder joint at a temperature of 180 °C for 480 h with ~2 *wt*% Fe-nanoparticles doped in flux: (a) Contour map, (b) averaging the statistics points for three different regions of the copper substrate, IMC layer, and solder joint, (c) line/2D, and (d) surface/3D distribution profiles, as combined with (e) FE-SEM microscopy images from the nano-indent impressions across the different parts of the solder joint.

a, b, and the distribution profiles of Figs. 17(I)c, d, for some regions inside the solder joint and near the interface, some degree of strengthening can be expressed; those could be due to the contribution of $Ag_3Sn$ intermetallic precipitation through the solder alloy matrix along with possible separated IMC pieces from the interface. Such localized mechanical response measurements are well consistent with the corresponding microstructural details of this material, as revealed before by FE-SEM as shown in Fig. 2a. As expected in the case of hybrid solder joint with incorporated reactive Fe-NPs after reflow solidification and thermal aging, hardness, and reduced modulus calculations by nanoindentation mapping in Figs. 18(I) and (II) revealed the contribution of the IMC layer along both sides of the solder joint with a thickness range between 10 and 20 μm.

Incorporation of reactive Fe-NPs results in a notable enhancement in the hardness of the solder joint interface, reaching approximately 10,000 MPa (~10 GPa), significantly surpassing that of the non-reinforced sample. This substantial increase in hardness is intricately linked to the proposed mechanistic models outlined in Figs. 15 and 16, which elucidate the contribution and impact of Fe-NPs primarily through nano-scale precipitation of the $FeSn_2$ phase within and in front of the $Cu_6Sn_5$ IMC layer. This nano-scale precipitation is attributed to inducing significant strengthening effects. Furthermore, the atomic diffusion of iron and subsequent alteration in the stoichiometry of the $Cu_6Sn_5$ compound, particularly toward the stability of the $(Cu, Fe)_6Sn_5$ phase, further contribute to the observed hardening.

Moreover, within the solder joint region, the presence of intermetallic $Ag_3Sn$ islands and precipitates dispersed throughout the Sn—Ag solder alloy matrix introduces fluctuations in mechanical stiffness across the solder joint area. The distribution of these complex phases leads to variations in mechanical properties, as evidenced by scattered points in the 3D distribution profiles depicted in Figs. 18(I)d and 18(II)d. To corroborate these findings, nanoindentation impressions were characterized through FE-SEM surface topography analysis under secondary electron imaging mode across different regions of the solder joint, including the copper substrate, IMC layers at the interface, and solder joint area, as illustrated in Fig. 18(I)e. These depth-controlled nanoindentation mapping measurements validate the successful execution of the characterization process, providing crucial insights into the mechanical behavior of the solder joint interface and the contributions of various reinforcing phases to its overall mechanical properties.

## 4. Conclusions

A comprehensive scientific investigation into the formation and

growth kinetics of intermetallic compound (IMC) layers during soldering, along with their potential interaction and retardation by secondary phase nanoparticles, represents a significant innovation within the described project. Advanced electron microscopy characterizations play a pivotal role in elucidating these processes. Diffusion calculations, based on IMC layer thickening at solder joint interfaces under varying aging conditions, reveal a higher activation energy of approximately 55 kJ/mol for the formation of the total IMC layer in the hybrid nanocomposite solder joint, compared to around 46 kJ/mol for the non-reinforced case. Integration of FIB/STEM analysis from the IMC layer interface with the solder alloy matrix, in conjunction with FE-SEM/EDS global mapping of Fe nanoparticles distribution around the interaction region, facilitates the elucidation of mechanisms underlying the suppression of IMC interface progression.

Detailed STEM/EDS examinations of distributed nano-scale precipitates within the solidified $Cu_6Sn_5$ IMC layer and its immediate vicinity unveil three distinct mechanisms contributing to this phenomenon. Firstly, iron diffusion within the IMC layer matrix alters its lattice stoichiometry toward $(Cu, Fe)_6Sn_5$ instead of $Cu_6Sn_5$. Secondly, the decomposition of iron nanoparticles within the reactive Sn—Ag molten solder alloy, followed by subsequent solid-state interfacial diffusion during post-annealing/aging treatments, potentially yields the formation of $FeSn_2$ phase, alongside partial iron segregation along boundaries. Nanoindentation mapping of hybrid and non-reinforced solder joints underscores the significant influence of reactive iron nanoparticles on solder joint formation, IMC layer development, and phase segregation, thereby controlling localized mechanical performance. A substantial hardening contribution of up to approximately 10 GPa at the interface of the hybrid solder joint is attributed to IMC layer formation and the notable contribution of reactive Fe nanoparticles, alongside the formation of dispersed $FeSn_2$ intermetallic nano-precipitates.

Table 1. Processing conditions regarding the preparation of different solder joints with incorporation of varying iron nanoparticle content at the interface doped into the flux before and after age-annealing heat treatments at various temperatures and times.

Table 2. The calculated values of the growth rate constant for the separate and simultaneous formation of IMC layers at two different aging temperatures of 120 and 180 °C for the altered contents of Fe-NPs.

Table 3. Comparison between the estimated activation energy ranges for the formation and growth of IMC layers.

## CRediT authorship contribution statement

**Farzad Khodabakhshi:** Writing – review & editing, Writing – original draft, Visualization, Validation, Software, Methodology, Investigation, Formal analysis, Data curation, Conceptualization. **Irina Wodak:** Methodology, Formal analysis, Data curation. **Andriy Yakymovych:** Methodology. **Shabnam Taheriniya:** Investigation. **Saba Khademorezaian:** Investigation. **Gerhard Wilde:** Writing – review & editing, Supervision, Resources. **Golta Khatibi:** Writing – review & editing, Writing – original draft, Visualization, Validation, Supervision, Resources, Project administration, Methodology, Funding acquisition, Data curation, Conceptualization.

## Declaration of competing interest

The authors declare that they have no known competing financial interests or personal relationships that could have appeared to influence the work reported in this paper.

## Data availability

Data will be made available on request.

## Acknowledgements

This research was funded in whole or in part by the Austrian Science Fund (FWF) [10.55776/P34894]. For open access purposes, the author has applied a CC BY public copyright license to any author-accepted manuscript version arising from this submission.

## References

[1] J. Bath, Lead-Free Soldering, Springer, US, 2007.
[2] J. Keller, D. Baither, U. Wilke, G. Schmitz, Mechanical properties of Pb-free SnAg solder joints, Acta Mater. 59 (7) (2011) 2731–2741.
[3] Y.W. Chang, Y. Cheng, F. Xu, L. Helfen, T. Tian, M. Di Michiel, C. Chen, K.N. Tu, T. Baumbach, Study of electromigration-induced formation of discrete voids in flip-chip solder joints by *in-situ* 3D laminography observation and finite-element modeling, Acta Mater. 117 (2016) 100–110.
[4] J. Shen, Y.C. Chan, S.Y. Liu, Growth mechanism of $Ni_3Sn_4$ in a Sn/Ni liquid/solid interfacial reaction, Acta Mater. 57 (17) (2009) 5196–5206.
[5] A. Luktuke, A.S.S. Singaravelu, A. Mannodi-Kanakkithodi, N. Chawla, Influence of indium addition on microstructural and mechanical behavior of Sn solder alloys: experiments and first principles calculations, Acta Mater. 249 (2023) 118853.
[6] A. Kodentsov, J. Wojewoda-Budka, L. Litynska-Dobrzynska, P. Zieba, A. Wierzbicka-Miernik, Formation of intermetallic compounds in reaction between cu–Ni alloys and solid Sn – a new look at the prominent effect of Ni, J. Alloys Compd. 858 (2021) 157677.
[7] T. Ventura, S. Terzi, M. Rappaz, A.K. Dahle, Effects of solidification kinetics on microstructure formation in binary Sn–cu solder alloys, Acta Mater. 59 (4) (2011) 1651–1658.
[8] O.Y. Liashenko, S. Lay, F. Hodaj, On the initial stages of phase formation at the solid cu/liquid Sn-based solder interface, Acta Mater. 117 (2016) 216–227.
[9] O.Y. Liashenko, F. Hodaj, Differences in the interfacial reaction between cu substrate and metastable supercooled liquid Sn–cu solder or solid Sn–cu solder at 222°C: experimental results versus theoretical model calculations, Acta Mater. 99 (2015) 106–118.
[10] J. Görlich, D. Baither, G. Schmitz, Reaction kinetics of Ni/Sn soldering reaction, Acta Mater. 58 (9) (2010) 3187–3197.
[11] K.H. Prakash, T. Sritharan, Interface reaction between copper and molten tin–lead solders, Acta Mater. 49 (13) (2001) 2481–2489.
[12] M. Abtew, G. Selvaduray, Lead-free Solders in Microelectronics, Mater. Sci. Eng. R. Rep. 27 (5) (2000) 95–141.
[13] M.S. Park, R. Arróyave, Early stages of intermetallic compound formation and growth during lead-free soldering, Acta Mater. 58 (14) (2010) 4900–4910.
[14] B.-J. Lee, N.M. Hwang, H.M. Lee, Prediction of interface reaction products between cu and various solder alloys by thermodynamic calculation, Acta Mater. 45 (5) (1997) 1867–1874.
[15] A. Durga, P. Wollants, N. Moelans, Phase-field study of IMC growth in Sn–cu/cu solder joints including elastoplastic effects, Acta Mater. 188 (2020) 241–258.
[16] M.S. Park, S.L. Gibbons, R. Arróyave, Phase-field simulations of intermetallic compound evolution in cu/Sn solder joints under electromigration, Acta Mater. 61 (19) (2013) 7142–7154.
[17] K.K. Hong, J.Y. Huh, Phase field simulations of morphological evolution and growth kinetics of solder reaction products, J. Electron. Mater. (2006) 56–64.
[18] G.J. Schmitz, B. Zhou, B. Böttger, S. Klima, J. Villain, Phase-field modeling and experimental observation of microstructures in solidifying Sn-ag-cu solders, J. Electron. Mater. 42 (8) (2013) 2658–2666.
[19] X.F. Tan, Q. Gu, M. Bermingham, S.D. McDonald, K. Nogita, Systematic investigation of the effect of Ni concentration in cu-xNi/Sn couples for high temperature soldering, Acta Mater. 226 (2022) 117661.
[20] M.S. Park, M.K. Stephenson, C. Shannon, L.A. Cáceres Díaz, K.A. Hudspeth, S. L. Gibbons, J. Muñoz-Saldaña, R. Arróyave, Experimental and computational study of the morphological evolution of intermetallic compound ($Cu_6Sn_5$) layers at the cu/Sn interface under isothermal soldering conditions, Acta Mater. 60 (13) (2012) 5125–5134.
[21] G. Zeng, S.D. McDonald, Q. Gu, Y. Terada, K. Uesugi, H. Yasuda, K. Nogita, The influence of Ni and Zn additions on microstructure and phase transformations in Sn–0.7Cu/cu solder joints, Acta Mater. 83 (2015) 357–371.
[22] N. Lu, D. Yang, L. Li, Interfacial reaction between Sn–ag–cu solder and co–P films with various microstructures, Acta Mater. 61 (12) (2013) 4581–4590.
[23] T. Ventura, S. Terzi, M. Rappaz, A.K. Dahle, Effects of Ni additions, trace elements and solidification kinetics on microstructure formation in Sn–0.7Cu solder, Acta Mater. 59 (10) (2011) 4197–4206.
[24] F. Khodabakhshi, M. Zareghomsheh, G. Khatibi, Nanoindentation creep properties of lead-free nanocomposite solders reinforced by modified carbon nanotubes, Mater. Sci. Eng. A 797 (2020) 140203.
[25] A. Roshanghias, A.H. Kokabi, Y. Miyashita, Y. Mutoh, I. Ihara, R.G. Guan Fatt, H. R. Madaah-Hosseini, Nanoindentation creep behavior of nanocomposite Sn-ag-cu solders, J. Electron. Mater. 41 (8) (2012) 2057–2064.
[26] A. Roshanghias, A.H. Kokabi, Y. Miyashita, Y. Mutoh, M. Rezayat, H.R. Madaah-Hosseini, Ceria reinforced nanocomposite solder foils fabricated by accumulative roll bonding process, J. Mater. Sci. Mater. Electron. 23 (9) (2012) 1698–1704.
[27] I.E. Anderson, J.L. Harringa, Suppression of void coalescence in thermal aging of tin-silver-copper-X solder joints, J. Electron. Mater. 35 (1) (2006) 94–106.

[28] T. Laurila, J. Hurtig, V. Vuorinen, J.K. Kivilahti, Effect of ag, Fe, au and Ni on the growth kinetics of Sn–cu intermetallic compound layers, Microelectron. Reliab. 49 (3) (2009) 242–247.
[29] M. Hutter, R. Schmidt, P. Zerrer, S. Rauschenbach, K. Wittke, W. Scheel, H. Reichl, Effects of additional elements (Fe, Co, Al) on SnAgCu solder joints, 2009 59th Electronic Components and Technology Conference, 2009, pp. 54–60.
[30] T. Laurila, V. Vuorinen, M. Paulasto-Kröckel, Impurity and alloying effects on interfacial reaction layers in Pb-free soldering, Mater. Sci. Eng. R. Rep. 68 (1) (2010) 1–38.
[31] A.S.M.A. Haseeb, M.M. Arafat, M.R. Johan, Stability of molybdenum nanoparticles in Sn–3.8Ag–0.7Cu solder during multiple reflow and their influence on interfacial intermetallic compounds, Mater. Charact. 64 (2012) 27–35.
[32] S.M.L. Nai, J. Wei, M. Gupta, Influence of ceramic reinforcements on the wettability and mechanical properties of novel lead-free solder composites, Thin Solid Films 504 (1–2) (2006) 401–404.
[33] A.S.M.A. Haseeb, M.M. Arafat, S.L. Tay, Y.M. Leong, Effects of metallic nanoparticles on interfacial intermetallic compounds in tin-based Solders for microelectronic packaging, J. Electron. Mater. 46 (10) (2017) 5503–5518.
[34] S.K. Ghosh, A.S.M.A. Haseeb, A. Afifi, Effects of metallic nanoparticle doped flux on interfacial intermetallic compounds between Sn-3.0Ag-0.5Cu and copper substrate, in: 2013 IEEE 15th Electronics Packaging Technology Conference (EPTC 2013), 2013, pp. 21–26.
[35] Y. Yang, J.N. Balaraju, Y. Huang, H. Liu, Z. Chen, Interface reaction between an electroless Ni–co–P metallization and Sn–3.5Ag lead-free solder with improved joint reliability, Acta Mater. 71 (2014) 69–79.
[36] N.S. Javid, R. Sayyadi, F. Khodabakhshi, Lead-free Sn-based/MW-CNTs nanocomposite soldering: effects of reinforcing content, Ni-coating modification, and isothermal ageing treatment, J. Mater. Sci. Mater. Electron. 30 (2019) 4737–4752.
[37] F. Khodabakhshi, R. Sayyadi, N.S. Javid, Lead free Sn-ag-cu solders reinforced by Ni-coated graphene nanosheets prepared by mechanical alloying: microstructural evolution and mechanical durability, Mater. Sci. Eng. A 702 (2017) 371–385.
[38] Y. Cui, J.W. Xian, A. Zois, K. Marquardt, H. Yasuda, C.M. Gourlay, Nucleation and growth of Ag3Sn in Sn-ag and Sn-ag-cu solder alloys, Acta Mater. 249 (2023) 118831.
[39] C.K. Chung, Y.J. Chen, W.M. Chen, C.R. Kao, Origin and evolution of voids in electroless Ni during soldering reaction, Acta Mater. 60 (11) (2012) 4586–4593.
[40] X. Deng, G. Piotrowski, J.J. Williams, N. Chawla, Influence of initial morphology and thickness of $Cu_6Sn_5$ and $Cu_3Sn$ intermetallics on growth and evolution during thermal aging of Sn-ag solder/cu joints, J. Electron. Mater. 32 (12) (2003) 1403–1413.
[41] L.M. Lee, A.A. Mohamad, Interfacial Reaction of Sn-ag-cu Lead-Free Solder Alloy on cu: A Review, Adv. Mater. Sci. Eng, 2013.
[42] H. Ma, J.C. Suhling, A review of mechanical properties of lead-free solders for electronic packaging, J. Mater. Sci. 44 (5) (2009) 1141–1158.
[43] D.A. Shnawah, M.F.M. Sabri, I.A. Badruddin, A review on thermal cycling and drop impact reliability of SAC solder joint in portable electronic products, Microelectron. Reliab. 52 (1) (2012) 90–99.
[44] G. Zeng, S. Xue, L. Zhang, L. Gao, W. Dai, J. Luo, A review on the interfacial intermetallic compounds between Sn-ag-cu based solders and substrates, J. Mater. Sci. Mater. Electron. 21 (5) (2010) 421–440.
[45] S. Kumar, C.A. Handwerker, M.A. Dayananda, Intrinsic and Interdiffusion in cu-Sn system, J. Phase Equilib. Diffus. 32 (4) (2011) 309–319.
[46] A. Ting Tan, A. Wen Tan, F. Yusof, Influence of nanoparticle addition on the formation and growth of intermetallic compounds (IMCs) in cu/Sn–ag–cu/cu solder joint during different thermal conditions, Sci. Technol. Adv. Mater. 16 (3) (2015) 033505.
[47] P. Babaghorbani, S.M.L. Nai, M. Gupta, Reinforcements at nanometer length scale and the electrical resistivity of lead-free solders, J. Alloys Compd. 478 (1–2) (2009) 458–461.
[48] S.L. Tay, A.S.M.A. Haseeb, M.R. Johan, P.R. Munroe, M.Z. Quadir, Influence of Ni nanoparticle on the morphology and growth of interfacial intermetallic compounds between Sn–3.8Ag–0.7Cu lead-free solder and copper substrate, Intermetallics 33 (2013) 8–15.
[49] Y. Yuan, Y. Guan, D. Li, N. Moelans, Investigation of diffusion behavior in cu–Sn solid state diffusion couples, J. Alloys Compd. 661 (2016) 282–293.
[50] A. Paul, C. Ghosh, W.J. Boettinger, Diffusion parameters and growth mechanism of phases in the cu-Sn system, Metall. Mater. Trans. A: Phys. 42 (4) (2011) 952–963.
[51] C.B. Lee, J.W. Yoon, S.J. Suh, S.B. Jung, C.W. Yang, C.C. Shur, Y.E. Shin, Intermetallic compound layer formation between Sn–3.5 mass %ag BGA solder ball and (cu, immersion au/electroless Ni–P/cu) substrate, J. Mater. Sci. Mater. Electron. 14 (8) (2003) 487–493.
[52] M.S. Park, R. Arróyave, Concurrent nucleation, formation and growth of two intermetallic compounds ($Cu_6Sn_5$ and $Cu_3Sn$) during the early stages of lead-free soldering, Acta Mater. 60 (3) (2012) 923–934.
[53] J. Gong, C. Liu, P.P. Conway, V.V. Silberschmidt, Evolution of CuSn intermetallics between molten SnAgCu solder and cu substrate, Acta Mater. 56 (16) (2008) 4291–4297.
[54] J.O. Suh, K.N. Tu, G.V. Lutsenko, A.M. Gusak, Size distribution and morphology of $Cu_6Sn_5$ scallops in wetting reaction between molten solder and copper, Acta Mater. 56 (5) (2008) 1075–1083.
[55] W. Yang, X. Quy Tran, T. Yamamoto, S. Yoshioka, F. Somidin, K. Nogita, S. Matsumura, Atomic locations of minor dopants and their roles in the stabilization of $\eta-Cu_6Sn_5$, Phys. Rev. Mater. 4 (6) (2020) 065002.
[56] X. Zhang, G. Ma, M. Liu, Micro-segregation model calculation of residual tin in boiler and pressure vessel steel, Philos. Mag. 99 (9) (2019) 1041–1056.
[57] L.Y. Gao, C.F. Li, P. Wan, H. Zhang, Z.Q. Liu, The diffusion barrier effect of Fe-Ni UBM as compared to the commercial cu UBM during high temperature storage, J. Alloys Compd. 739 (2018) 632–642.